International Journal of Mechanical Sciences 309 (2026) 111038

Contents lists available at ScienceDirect

International Journal of Mechanical Sciences

journal homepage: www.elsevier.com/locate/ijmecsci

Dispersion properties of guided elastic waves in micropolar plates

Annamaria Pau [a], Marco Lepidi [b,*]

[a] Sapienza University of Rome - Department of Structural and Geotechnical Engineering, Via Eudossiana 18, 00184 Rome, Italy
[b] University of Genoa - Department of Civil, Chemical and Environmental Engineering, Via Montallegro 1, 16145 Genoa, Italy

ARTICLE INFO

Keywords:
Cosserat continuum
Acoustic tensor
Wave propagation
Dispersion spectrum
Partial wave technique
Veering phenomenon
Modal hybridization

ABSTRACT

The free propagation of harmonic guided waves in homogeneous isotropic micropolar plates is investigated. The physical–mathematical model treats the micropolar plates as finite-thickness layers of linearly elastic Cosserat continuum, bounded by traction-free parallel planes. Initially, the partial differential equations governing free undamped motion are formulated for the unbounded three-dimensional micropolar continuum. Their analytical solutions are obtained by an original spectral decomposition of the acoustic tensor in the frequency domain. The resulting dispersion spectrum is endowed with spectral branches – absent in the classical Cauchy continuum –, which are associated with microrotational waveforms and characterized by distinct cutoff frequencies. A novel energy-based criterion is proposed to classify and quantify the waveform polarization. Subsequently, the partial wave method is employed to enforce boundary conditions and to construct semi-analytical solutions for the elastodynamic problem of harmonic guided waves propagating in infinite plates. This analysis enables a comprehensive characterization of the dispersion properties for both in-plane and out-of-plane uncoupled problems. From a mechanical perspective, the parametric analyses of the in-plane problem solutions reveal significant qualitative and quantitative effects of micropolarity on wave dynamics. In addition to the spectral enrichment due to micropolar branches, several distinctive dynamic phenomena are identified and parametrically described. These include frequency hardening, non-dispersive behavior in the limits of long/short wavelengths, asymptotic coalescence of phase/group speeds, proliferation of internal resonances, crossing and veering of spectral branches, hybridization of quasi-resonant translational and microrotational wavemodes. Mathematical conditions for the occurrence of frequency veering and modal hybridization are established.

1. Introduction

In a micropolar continuum, the configuration of each material particle is described by six degrees of freedom, including three translations and three rotations. The idea of considering the rotational degrees of freedom as independent variables was presented in the landmark work by the Cosserat brothers at the beginning of the twentieth century [1]. This seminal study summarized and enveloped the early contributions of Kirchhoff, Clebsh, Duhem, Voigt and Poincaré [2], which emerged from foundational discussions on the principles of energy balance, in particular the balance of momentum of momentum, dating back to the pioneering intuitions of Lagrange, Euler, and Bernoulli. Since the 1950s of the last century, the interest of the scientific community in the conceptual framework outlined by the Cosserats, and fostered by the influential contributions of eminent scholars [3–5], has grown exponentially. The initial development of micropolar continuum models was principally motivated by physical considerations, particularly the necessity to completely characterize the rich kinematics of granular assemblies and particulate matter. Indeed, the specification of dynamic configurations of such materials mandates the introduction of additional kinematic descriptors that can account for the intrinsic orientation, or polarity, of individual grains or particles. As the theoretical background of micropolar kinematics has progressively matured over the years, its applicability has been extended to a large variety of solids that can be idealized as continuous manifolds of infinitesimal rigid bodies, such as crystalline compounds, consolidated soils, fiber-reinforced concretes, multi-phasic composites [6–9]. Furthermore, micropolar models are commonly applied to inhomogeneous media with porosities, inclusions or cracks [10,11], large molecule polymers such as cellular foams [12,13], repetitive beam grids and regular masonries [14,15], biological tissues and their biomimetic counterparts [16,17]. Recently, functionally graded micropolar models have been proposed as energetically equivalent representations of semiperiodic or even aperiodic mesostructures [18]. Nowadays, with the extraordinary advent of multiscale architected

* Corresponding author.
E-mail addresses: annamaria.pau@uniroma1.it (A. Pau), marco.lepidi@unige.it (M. Lepidi).

https://doi.org/10.1016/j.ijmecsci.2025.111038
Received 18 September 2025; Received in revised form 23 October 2025; Accepted 14 November 2025
Available online 20 November 2025

materials and composite periodic metamaterials, these original motivations are strengthened – and in some cases overshadowed – by the need to introduce micropolarity as an indispensable property of homogenized continua, capable of reproducing at the macroscale the peculiar mechanical behavior of repetitive microstructures, such as brickwork masonries, chiral beam lattices, block-lattice systems [19–23]. Specifically, in vibration mechanics, the use of enriched micropolar descriptions becomes indispensable in problems characterized by wavelengths and frequencies of the same order of magnitude of the internal characteristic length and of the inverse of the internal characteristic time [24–29]. Taking micropolarity into account has also proved to be essential for the discovery, theoretical characterization and experimental verification of new dynamical phenomena, related to the dispersive nature of micropolar media, such as the emergence of roton-like minima in the acoustic branches of the dispersion spectrum, caused by ultra strong rototranslational coupling and phonon mode hybridization [30,31].

In accordance with the mechanical principle of duality, adjacent particles within a micropolar continuum are postulated to interact by independent contact forces and moment couples. Consequently, infinitesimal internal volumes exchange not only classical stresses, but also couple stresses (also referred to as microcouple stresses) across the interfacial area. From the equilibrium equations governing an infinitesimal volume element, it follows that neither the stress tensor nor the microcouple stress tensor can, in general, be assumed to possess symmetry. Following the resurgence of interest in Cosserat's theoretical background in the mid-20th century, first investigations focused on an intermediate formulation, commonly referred to as the *Cosserat pseudocontinuum*. This simplified model incorporates asymmetric stress and couple stress tensors, yet describes deformations solely through the translational displacement field, treating microrotations as dependent variables [32–35]. It required approximately two decades of further theoretical refinements for the model to evolve into the comprehensive and fully developed form recognized in contemporary continuum mechanics [36–41].

Despite the linear theory of micropolar continua has already reached a high grade of formal rigor, mathematical elegance, and internal coherence, one of the main deterrents to its widespread adoption remains the identification and determination of its material parameters. Even in the simplest isotropic case, the constitutive model requires a data-driven evaluation of six independent material constants. This challenging point is further compounded by the inherent non-periodicity of the internal microstructure in most solids, which complicates the homogenization and parameter identification processes [25]. In practice, the limited availability of reliable data on these constants has significantly restricted the implementation of micropolar models [42]. Although some studies have addressed the experimental determination of these parameters – occasionally leveraging dynamic response data – such efforts remain relatively limited [16,43–46]. In dynamic formulations, the inclusion of rotational microinertia introduces additional parameters, thereby further increasing the complexity of experimental calibration.

In parallel with the growing spreading of the Cosserat theory, the fundamental principles governing the propagation of linear elastic waves in micropolar continua were being established. Among the earliest relevant findings within the context of micropolar Cosserat pseudocontinua, the speed of longitudinal waves was found to be independent of the oscillation frequency, while the speeds of all bulk waves differ from one another [35]. Notably, in contrast to wave propagation in classical Cauchy continua, bulk waves in micropolar media exhibit cutoff frequencies, below which propagation is inhibited [34]. Furthermore, the theory predicted the emergence of new types of waves absent in classical elasticity. By adopting the complete linear theory of Cosserat elasticity, the existence of distinct wave types – namely longitudinal (uncoupled displacement and microrotation), and transversal (coupled displacement/microrotation) – was recognized, and respective cutoff frequencies were determined [38]. The principal outcomes from this substantial body of research, developed primarily in the late 1960s, are synthesized and discussed in Parfitt and Eringen [47], which also includes investigations into the interaction of bulk waves with planar interfaces. The analytical derivation of dispersion relations in Cosserat continua is also detailed in Kulesh et al. [48]. More recently, the remarkable effects of micropolarity on the free propagation and dispersion of harmonic waves have been highlighted through comparative studies between the classical Cauchy model and the so-called *reduced Cosserat model*, in which the stress tensor is asymmetric, but the couple stress tensor vanishes [49,50].

Starting from this physical–mathematical background, the present study addresses the propagation of elastic waves in a micropolar plate, idealized as an infinite homogeneous isotropic layer of Cosserat continuum with finite-thickness, bounded by two parallel traction-free planes. Particular emphasis is placed on clarifying the role of microstructural effects in shaping the characteristics of guided wave modes. An early attempt to formulate this problem was presented in Gauthier and Jahsman [51], where a strong simplifying assumption is introduced by neglecting certain terms in the characteristic equation, and no analysis of modal waveforms is carried out. Subsequently, Eringen [25] advanced the solution of the problem by providing a qualitative picture of the dispersion properties and the complete expression of the characteristic equations for the symmetric and antisymmetric modes. Later, Kulesh et al. [52] contributed further by depicting the dispersion relations and identifying some quantitative features of wave propagation in micropolar waveguides. While the analogous problem in classical Cauchy continua is well established and its solutions are thoroughly documented in the literature – see, for instance, the textbooks by Rose [53] and Auld [54], as well as studies addressing cases without cubic material symmetry [55] or with viscous dissipation [56–58] – the corresponding analysis in micropolar media remains comparatively limited in both scope and dissemination, with fewer references available, to the best of the authors' knowledge.

The principal scientific motivation for filling this research gap is that the propagation of elastic waves in micropolar plates encompasses a wide range of interesting physical phenomena, including the asymptotic behavior in the limits of long and short wavelengths, the morphological modification of the standing waveforms, the parameter-dependent occurrence of internal resonance conditions, the inter-wave transfer of mechanical energy. In the authors' opinion, part of these aspects has eluded previous initiatives of investigation and remain only partially explored and/or understood. Unfolding such complex phenomena may not only provide new insights into the theoretical understanding of the role played by micropolarity in wave dynamics, but also disclose new potentialities in stating and solving novel direct and inverse (identification) problems. Based on this motivating standpoint, the paper focuses on harmonic guided waves propagating periodically with small oscillation amplitudes in non dissipative Cosserat plates. From the methodological viewpoint, the problem specification for infinite plate waveguides has been addressed in the frequency-wavevector domain through the versatile partial wave technique [55,59–61]. Since the resulting dispersion properties of the micropolar continuum differ markedly from those of a classical Cauchy continuum, the first objective is to investigate the qualitative and quantitative impact of the micropolar parameters on the propagation characteristics. Most importantly, the dispersion spectrum is enriched by a distinct class of spectral branches, associated with pure microrotational waves, which are unique to the micropolar continuum. Consequently, a complementary objective is the complete characterization of the new spectral branches, by tracking how their frequency, their phase or group speeds and their waveform morphology evolve as a function of the wavevector, with special focus on the limits of short and long wavelengths. The final objective is the local analysis and phenomenological description of the internal resonance conditions that emerge from the intersections of the micropolar spectral branches with the classical branches of the

spectrum. Particularly noteworthy are the quasi-resonance regions of the dispersion spectrum where a micropolar spectral branch activates modal mechanisms of linear interaction with other spectral branches. Since the modal interplay in resonance conditions enables inter-wave transfers of mechanical energy, the identification of the resonant regions in the frequency domain and the parameter space, as well as the physical interpretation of the linear interaction mechanisms, may pave the way for the indirect excitation and experimental observation of some of the most elusive characteristics of micropolar continua.

The paper is organized in four sections. After the Introduction, Section 2 presents the most general formulation of the problem, dealing with the propagation of plane bulk waves in an unbounded infinite micropolar continuum. A fully analytical spectral decomposition of the acoustic tensor is proposed. Characteristic relations governing the free dynamics of the material, independently of boundary effects, are analytically derived. An energy-based polarization factor is proposed to quantitatively evaluate the coupling between displacement and microrotation fields. Section 3 builds upon this general formulation by introducing geometric confinement and specifying boundary conditions, thus extending the analysis to finite-thickness plate waveguides. In this framework, the partial wave technique is employed to enforce stress-free conditions on the external surfaces and state the dispersion problem for guided harmonic waves. Section 4 completes the hierarchical sequence of dynamic problems by focusing on in-plane guided waves, which represent an independent subset of solutions for the dispersion problem stated in Section 3. Both primary dispersion properties – like wavefrequencies and waveforms – and secondary dispersion properties – like phase and group speeds – are determined. A detailed analysis of the results is provided, highlighting micropolar spectral branches, crossing and veering of dispersion curves, and hybridization of resonant waveforms. Concluding remarks are finally provided. The definitions of functions and differential operators necessary for an effortless understanding of the text are reported in Appendix.

2. Free wave propagation in infinite micropolar solids

The physical–mathematical formulation of the free vibration problem for the micropolar continuum is based on the Eringen's theory of linear micropolar elasticity [62]. The fundamental hypothesis asserts that each particle point P of the micropolar continuum is both displaceable and orientable [63,64]. Consequently, in the three-dimensional space spanned by Cartesian coordinates running along the orthogonal base vectors $\mathbf{e}_i$ (with $i = 1, 2, 3$), the reference natural configuration $\mathcal{B}$ of a micropolar deformable solid is defined by the position vector $\mathbf{X}$ and the orientation trihedron of orthonormal directors $\mathbf{D}_i$, attributed to each particle point at the initial time instant. During the motion, the actual configuration $\mathcal{B}'$ is defined not only by the time-dependent field of position vector $\mathbf{x}(\mathbf{X}, t)$, but also by the three time-dependent fields of directors $\mathbf{d}_i(\mathbf{X}, t)$, which are allowed to rotate without losing their mutual orthogonality. Therefore, the change of configuration is described by the displacement vector field $\mathbf{u}(\mathbf{X}, t)$ and by the microrotation tensor field $\mathbf{H}(\mathbf{X}, t)$, reading

$$\mathbf{u}(\mathbf{X}, t) = \mathbf{x}(\mathbf{X}, t) - \mathbf{X}, \qquad \mathbf{H}(\mathbf{X}, t) = \mathbf{d}_i(\mathbf{X}, t) \otimes \mathbf{D}_i, \tag{1}$$

where $\otimes$ indicates the tensor product and summation is understood over the repeated index i, according to the Einstein notation. In general, the microrotation tensor field $\mathbf{H}(\mathbf{X}, t)$ is a nonlinear function of the microrotation vector field $\boldsymbol{\theta}(\mathbf{X}, t)$, which is assumed to be independent of the displacement field $\mathbf{u}(\mathbf{X}, t)$. Physically, the micropolar continuum has three translational degrees-of-freedom $u_i(\mathbf{X}, t)$, like the classical continuum, plus three orientational degrees-of-freedom $\theta_i(\mathbf{X}, t)$, representing the microrotations around the axes $\mathbf{e}_i$. In the linear theory, displacements and microrotations are assumed to be small (together with their derivatives), so that the vector fields $\mathbf{u}(\mathbf{X}, t)$ and $\boldsymbol{\theta}(\mathbf{X}, t)$ are regarded as infinitesimal displacements and infinitesimal microrotations, respectively. Accordingly, the infinitesimal microrotation tensor assumes the non-symmetric form

$$\boldsymbol{\eta}(\mathbf{X}, t) = \begin{bmatrix} 1 & -\theta_3(\mathbf{X}, t) & \theta_2(\mathbf{X}, t) \\ \theta_3(\mathbf{X}, t) & 1 & -\theta_1(\mathbf{X}, t) \\ -\theta_2(\mathbf{X}, t) & \theta_1(\mathbf{X}, t) & 1 \end{bmatrix}, \tag{2}$$

so that the vector $\boldsymbol{\theta} = (\theta_1, \theta_2, \theta_3)^\top$ of (small) microrotations plays also the role of axial vector for the skew-symmetric tensor $\boldsymbol{\Theta} = \boldsymbol{\eta} - \mathbf{I} = -\sum_{i,j,k}^{3} (\in_{ijk} \mathbf{e}_i \otimes \mathbf{e}_j \otimes \mathbf{e}_k)\boldsymbol{\theta}$ (as defined in the Appendix).

The geometrical deformation occurring during configurational changes of micropolar solids can be described by introducing the Lagrangian stretch tensor $\mathbf{E}(\mathbf{X}, t)$ and the wryness tensor $\mathbf{K}(\mathbf{X}, t)$, whose natural definitions (see for instance [65]) are

$$\mathbf{E}(\mathbf{X}, t) = \mathbf{H}(\mathbf{X}, t)^\top \big(\mathbf{I} + \nabla \mathbf{u}(\mathbf{X}, t)\big) - \mathbf{I}, \qquad \mathbf{K}(\mathbf{X}, t) = \mathbf{g}_i(\mathbf{X}, t) \otimes \mathbf{e}_i, \tag{3}$$

where ∇ indicates gradient operator with respect to the spatial coordinates, while $\mathbf{g}_i(\mathbf{X}, t)$ is the axial vector of the skew-symmetric tensor $\mathbf{G}_i = \mathbf{H}^\top \partial \mathbf{H} / \partial X_i$. Under the assumption of small displacements and microrotations, the stretch and wryness tensors assume the linear form

$$\boldsymbol{\epsilon}(\mathbf{X}, t) = \nabla \mathbf{u}(\mathbf{X}, t) - \boldsymbol{\Theta}(\mathbf{X}, t), \qquad \boldsymbol{\kappa}(\mathbf{X}, t) = \nabla \boldsymbol{\theta}(\mathbf{X}, t), \tag{4}$$

which serve also as governing equations ruling the relationship between the deformation descriptors $\boldsymbol{\epsilon}$ (strain tensor) and $\boldsymbol{\kappa}$ (microcurvature tensor) and the displacement variables $\mathbf{u}$ and $\boldsymbol{\theta}$. In boundary value problems, Eqs. (4) hold on the entire volume $\mathcal{V}_\mathcal{B}$ occupied by the micropolar body in the reference configuration, and are supplemented by boundary conditions $\mathbf{u} = \mathbf{0}$ and $\boldsymbol{\theta} = \mathbf{0}$ applied on the fixed part of the frontier $\partial \mathcal{V}_u$.

Within the linear theory of micropolar continua, the superficial interactions between any two complementary body parts are described by the stress vector $\mathbf{t}_n(\mathbf{X}, t) = \mathbf{t}(\mathbf{X}, \mathbf{n}, t)$, like in the classical continuum, and the couple stress vector $\mathbf{m}_n(\mathbf{X}, t) = \mathbf{m}(\mathbf{X}, \mathbf{n}, t)$. The unit vector $\mathbf{n}$ is the normal to the part-separating surface $\mathcal{S}_n$. Therefore the stress vector $\mathbf{t}_n$ and couple stress vector $\mathbf{m}_n$ can be intended as the contact force and couple, respectively, per unit area of the surface $\mathcal{S}_n$ passing through the particle point P. For the generic position $\mathbf{X}$, the stress vector and the couple stress vector are postulated to depend only on the normal $\mathbf{n}$, according to the extended Cauchy theorems

$$\mathbf{t}_n = \mathbf{S}\mathbf{n}, \qquad \mathbf{m}_n = \mathbf{W}\mathbf{n}, \tag{5}$$

where $\mathbf{S}$ and $\mathbf{W}$ are the non-symmetric stress and couple stress tensors, respectively.

According to the Euler's laws of motion, the applied force on a volume $\mathcal{V}$ equals the rate of change of linear momentum of $\mathcal{V}$ and the applied couple equals the rate of change of momentum of momentum. This is equivalent to require that the balance of momentum and of momentum of momentum are satisfied for all infinitesimal volumes. Consequently, in the specific case of isotropic micropolar continuum under the effects of no other loads except inertial forces, the dynamic equilibrium equations are

$$\operatorname{div} \mathbf{S} = \rho \ddot{\mathbf{u}}, \qquad \operatorname{div} \mathbf{W} + 2\,\mathbf{s} = \rho J \ddot{\boldsymbol{\theta}}, \tag{6}$$

where ρ and ρJ are the mass density and the rotatory inertia (of the particle points), respectively. The differential operator div indicates divergence, while the double dot represents second derivative with respect to time. The quantity $\mathbf{s}$ is the axial vector of the antisymmetric part of the stress tensor $\mathbf{S}^{\mathsf{A}} = \operatorname{skew}(\mathbf{S})$. In boundary-value problems for homogeneous bodies, Eqs. (6) are imposed on the entire volume $\mathcal{V}_\mathcal{B}$, and are supplemented by boundary conditions $\mathbf{t}_n = \mathbf{S}\mathbf{n}_f = \mathbf{0}$ and $\mathbf{m}_n = \mathbf{W}\mathbf{n}_f = \mathbf{0}$ applied on the unconstrained part of the frontier $\partial \mathcal{V}_f$ with normal $\mathbf{n}_f$.

Under the hypothesis of linear elasticity, the constitutive equations for the isotropic micropolar continuum can be expressed as a pair of

uncoupled relations between the linear stress and strain tensors, and the couple stress and microcurvature tensors (see [47,64])

$$\mathbf{S} = \lambda(\mathrm{tr}\,\boldsymbol{\epsilon})\mathbf{I} + 2\mu\,\boldsymbol{\epsilon}^{\mathrm{S}} + \kappa\,\boldsymbol{\epsilon}, \qquad \mathbf{W} = \alpha(\mathrm{tr}\,\boldsymbol{\kappa})\mathbf{I} + \beta\,\boldsymbol{\kappa}^{\top} + \gamma\,\boldsymbol{\kappa}, \tag{7}$$

where $\boldsymbol{\epsilon}^{\mathrm{S}} = \mathrm{sym}(\boldsymbol{\epsilon})$ is the symmetric part of the linear strain tensor. The quantities $\lambda, \mu, \alpha, \beta, \gamma, \kappa$ are the material moduli, which are constant in homogeneous bodies and must satisfy the inequalities

$$\begin{aligned} &3\lambda + 2\mu + \kappa \geq 0, \qquad &&2\mu + \kappa \geq 0, \qquad &&\kappa \geq 0, \\ &3\alpha + \beta + \gamma \geq 0, \qquad &&\beta + \gamma \geq 0, \qquad &&\gamma - \beta \geq 0, \end{aligned} \tag{8}$$

for the sake of thermodynamical consistency [39,64,66]. In principle, the six independent material moduli can be identified through data-driven approaches, although the direct experimental determination of the four micropolar parameters $\alpha, \beta, \gamma, \kappa$, as well as the rotational inertia ρJ, remains a challenging task [16,43,46]. On the other hand, in micropolar models derived from the continualization or homogenization of architected materials, elastic moduli do not correspond to intrinsic properties of the microscopic constituents, but rather represent effective macroscopic parameters that reflect the mechanical influence of the underlying periodic microstructure.

2.1. Equations of motion

The linear elastic problem related to the free undamped dynamics of the micropolar continuum can be tackled according to the displacement method, by selecting the displacement and microrotation fields as principal unknowns. By operating successive substitutions, the coupled equations of motion governing the regime of small amplitude oscillations finally read

$$\begin{aligned} &(\mu + \kappa)\nabla^2\mathbf{u} + (\lambda + \mu)\nabla(\mathrm{div}\,\mathbf{u}) + \kappa\ \mathrm{curl}\,\boldsymbol{\theta} = \rho\,\ddot{\mathbf{u}}, \\ &\gamma\nabla^2\boldsymbol{\theta} + (\alpha + \beta)\nabla(\mathrm{div}\,\boldsymbol{\theta}) + \kappa\ \mathrm{curl}\,\mathbf{u} - 2\kappa\,\boldsymbol{\theta} = \rho J\,\ddot{\boldsymbol{\theta}}, \end{aligned} \tag{9}$$

where curl and ∇^2 stand for the rotor and the Laplacian operators, respectively. In boundary-value problems, the equations of motion (valid in the volume $\mathcal{V}_B$) are supplemented by kinematic boundary conditions $\mathbf{u} = \mathbf{0}$ and $\boldsymbol{\theta} = \mathbf{0}$ (in $\partial\mathcal{V}_u$) and mechanical boundary conditions $[\lambda(\mathrm{div}\,\mathbf{u})\mathbf{I} + 2\mu\,\mathrm{sym}(\nabla\mathbf{u}) + \kappa(\nabla\mathbf{u} - \boldsymbol{\Theta})]\mathbf{n}_f = \mathbf{0}$ and $[\alpha\,\mathrm{tr}(\nabla\boldsymbol{\theta})\mathbf{I} + \beta\,\nabla\boldsymbol{\theta}^{\top} + \gamma\,\nabla\boldsymbol{\theta}]\mathbf{n}_f = \mathbf{0}$ (in $\partial\mathcal{V}_f$).

2.2. Plane waves in infinite Cosserat media

The homogeneous linear equations of motion (9) admit solutions in the class of plane waves oscillating harmonically – in time – with real-valued wavefrequency ω while propagating periodically – in space – along the direction of versor $\mathbf{n} = (n_1, n_2, n_3)^{\top}$ with wavevector $\mathbf{k} = k\mathbf{n} = (k_1, k_2, k_3)^{\top}$. Progressive waves advancing the positive $\mathbf{n}$-direction can be expressed as

$$\begin{aligned} &\mathbf{u}(\mathbf{x}, t) = \mathbf{a}\,\mathrm{e}^{I(\mathbf{k}\cdot\mathbf{x} - \omega t)} + cc, \\ &\boldsymbol{\theta}(\mathbf{x}, t) = \mathbf{b}\,\mathrm{e}^{I(\mathbf{k}\cdot\mathbf{x} - \omega t)} + cc, \end{aligned} \tag{10}$$

where $\mathbf{a}$ and $\mathbf{b}$ are complex amplitude vectors, I is the imaginary unit and cc stands for complex conjugate. Substitution of solution (10) into Eqs. (9) leads to the algebraic eigenproblem

$$\begin{aligned} &k^2\left[(\lambda + 2\mu + \kappa)\mathring{\mathbf{N}}\mathbf{a} + (\mu + \kappa)(\mathbf{I} - \mathring{\mathbf{N}})\mathbf{a} - I\kappa/k(\mathbf{n}\times\mathbf{b})\right] = \rho\,\omega^2\mathbf{a}, \\ &k^2\left[(\Sigma + 2\kappa/k^2)\mathring{\mathbf{N}}\mathbf{b} + (\gamma + 2\kappa/k^2)(\mathbf{I} - \mathring{\mathbf{N}})\mathbf{b} - I\kappa/k(\mathbf{n}\times\mathbf{a})\right] = \rho J\,\omega^2\mathbf{b}, \end{aligned} \tag{11}$$

where $\Sigma = \alpha + \beta + \gamma$ is a constitutive quantity depending on the material, $\mathring{\mathbf{N}} = \mathbf{n}\otimes\mathbf{n}$ is a three-by-three symmetric matrix and the symbol $\otimes$ stands for tensor product.

The eigenproblem (11) can be written in the compact *non-standard* form as $\mathbf{K}_n(k)\boldsymbol{\phi} = \omega^2\mathbf{M}\boldsymbol{\phi}$, where the eigenvector is $\boldsymbol{\phi} = (\mathbf{a}, \mathbf{b})$, the generalized k-dependent stiffness matrix $\mathbf{K}_n(k)$ is Hermitian, while the mass matrix $\mathbf{M}$ is diagonal. Therefore, by adopting the (unique) decomposition of the mass matrix $\mathbf{M} = \mathbf{Q}^{\top}\mathbf{Q}$ and introducing the linear change of variable $\boldsymbol{\phi} = \mathbf{Q}^{-1}\boldsymbol{\varphi}$, the eigenproblem can be transformed in the convenient *standard* form $(\mathbf{A}_n(k) - \omega^2\mathbf{I})\boldsymbol{\varphi} = \mathbf{0}$. The $\mathbf{n}$-dependent quantity $\mathbf{A}_n(k) = \mathbf{Q}^{-\top}\mathbf{K}_n(k)\mathbf{Q}^{-1}$ is defined *acoustic tensor* and has the peculiar parametric expression

$$\begin{aligned} \mathbf{A}_n(k) = \frac{k^2}{\rho}&\begin{bmatrix} (\lambda + 2\mu + \kappa)\mathring{\mathbf{N}} & \mathbf{O} \\ \mathbf{O} & (\Sigma + 2\kappa/k^2)/J\mathring{\mathbf{N}} \end{bmatrix} + \\ + \frac{k^2}{\rho}&\begin{bmatrix} (\mu + \kappa)(\mathbf{I} - \mathring{\mathbf{N}}) & -I\kappa/(k\sqrt{J})\mathbf{N} \\ -I\kappa/(k\sqrt{J})\mathbf{N} & (\gamma + 2\kappa/k^2)/J(\mathbf{I} - \mathring{\mathbf{N}}) \end{bmatrix}, \end{aligned} \tag{12}$$

which preserves the Hermitian properties. The versor $\mathbf{n}$ is regarded as *axial vector* of the skew-symmetric matrix $\mathbf{N} = -\sum_{i,j,k}^{3}(\in_{ijk}\,\mathbf{e}_i\otimes\mathbf{e}_j\otimes\mathbf{e}_k)\mathbf{n}$.

Solving the eigenproblem consists in determining the six eigenpairs $(\omega^2, \boldsymbol{\varphi})$, where the square quantity ω^2 serves as unknown eigenvalue and $\boldsymbol{\varphi} = (\boldsymbol{\varphi}_a, \boldsymbol{\varphi}_b)$ plays the role of unknown standard eigenvector, related to the non-standard eigenvector $\boldsymbol{\phi}$ by the inverse change of coordinates $\boldsymbol{\varphi} = \mathbf{Q}\boldsymbol{\phi}$. Since the matrix $\mathbf{Q}$ is diagonal, the change of coordinates preserves vector collinearities and orthogonalities. According to the so-called *inverse method* (see [67]), once a certain eigenpair $(\omega^2, \boldsymbol{\varphi})$ is known as a function of the wavenumber k, adopted as free positive real-valued parameter, the eigenvalue $\omega^2(k)$ provides the dispersion relation $\omega(k)$ characterizing the plane wave harmonically oscillating in time with circular frequency ω while propagating in space with wavenumber k. The associated eigenvector $\boldsymbol{\phi}(k) = \mathbf{Q}^{-1}\boldsymbol{\varphi}(k)$ describes the propagating waveform, whose amplitude remains undetermined. Subvectors $\boldsymbol{\varphi}_a(k)$ and $\boldsymbol{\varphi}_b(k)$ collect the eigendisplacements and eigenrotations, respectively, participating in the eigenvector $\boldsymbol{\varphi}(k)$. The curve representing the function $\omega(k)$ in the frequency–wavenumber space is a branch of the spectral diagram. Packets of waves propagate with phase speed $c(k) = \omega(k)/k$ and group speed $g(k) = \partial\omega(k)/\partial k = c(k) + k\,\partial c(k)/\partial k$, so that dispersion actually occurs if $\partial c(k)/\partial k \neq 0$. According to the alternative *direct method*, the frequency ω can be assumed as free positive real-valued parameter (to respect the assumption of progressive waves), while the square wavenumber k^2 plays the role of eigenvalue. Consequently, the eigensolution provides the dispersion relation in the direct form $k(\omega)$. The direct dispersion function discloses that the range of frequencies ω corresponding to real-valued wavenumbers $k(\omega)$ identifies the spectral passband allowing the free wave propagation. On the contrary, the range of frequencies ω corresponding to imaginary-valued wavenumbers $k(\omega)$ identifies the spectral stopband inhibiting the free wave propagation.

The two-termed expression (12) can be recognized as a spectral decomposition of tensor $\mathbf{A}_n$. Based on the Spectral Theorem and recalling the tensor Hermitianity, it can be proved that the tensor $\mathbf{A}_n$ has a complete eigenspace, characterized – for the generic wavenumber k – by four distinct real-valued eigenvalues ω_i^2 (corresponding to four positive-valued circular frequencies ω_i to satisfy the assumption of progressive waves) and six distinct eigenvectors $\boldsymbol{\varphi}_i$, orthogonal to each other. Specifically, the tensor has two single eigenvalues ω_1^2 and ω_2^2 (respectively associated to unique eigenvectors $\boldsymbol{\varphi}_1$ and $\boldsymbol{\varphi}_2$) and two multiple non-defective eigenvalues ω_3^2 and ω_5^2 with double algebraic and geometric multiplicity (respectively associated to eigenvector pairs $\boldsymbol{\varphi}_3$, $\boldsymbol{\varphi}_4$ and $\boldsymbol{\varphi}_5$, $\boldsymbol{\varphi}_6$). The two single eigenvalues can be identified from the first term of tensor $\mathbf{A}_n$ as

$$\omega_1^2(k) = \frac{k^2}{\rho}(\lambda + 2\mu + \kappa), \qquad \omega_2^2(k) = \frac{k^2}{\rho J}(\Sigma + 2\kappa/k^2), \tag{13}$$

while the remaining two double eigenvalues can be identified from the second term of tensor $\mathbf{A}_n$ as the real-valued solutions of a quadratic characteristic equation, reading

$$\omega_{3,5}^2(k) = \frac{2\kappa + k^2\left(\gamma + J(\kappa + \mu)\right) \mp \Delta_1(k)}{2\rho J}, \tag{14}$$

where $\Delta_1^2(k) = 4\kappa^2k^2J + \left[2\kappa + k^2\left(\gamma - J(\kappa + \mu)\right)\right]^2$ is a positive quantity by construction, which does not vanish in the entire k-domain as long as κ is strictly positive.

Table 1
Finite values of the dispersion functions for frequency $\omega(k)$, phase speed $c(k)$ and group speed $g(k)$ in the limits of short and long wavelengths.

	$i=1$	$i=2$	$i=3$	$i=5$
$\lim_{k\to 0^+}\omega_i(k)$	0	$\omega_2^\circ=\sqrt{\frac{2\kappa}{J\rho}}=\omega_c$	0	$\omega_5^\circ=\sqrt{\frac{2\kappa}{J\rho}}=\omega_c$
$\lim_{k\to\infty}\omega_i(k)$	-	-	-	-
$\lim_{k\to 0^+}c_i(k)$	$c_1^\circ=\sqrt{\frac{\kappa+\lambda+2\mu}{\rho}}$	-	$c_3^\circ=\sqrt{\frac{\kappa+2\mu}{2\rho}}$	-
$\lim_{k\to\infty}c_i(k)$	$c_1^\infty=\sqrt{\frac{\kappa+\lambda+2\mu}{\rho}}$	$c_2^\infty=\sqrt{\frac{\alpha+\beta+\gamma}{J\rho}}$	$c_3^\infty=\sqrt{\frac{\kappa+\mu}{\rho}}$	$c_5^\infty=\sqrt{\frac{\gamma}{J\rho}}$
$\lim_{k\to 0^+}g_i(k)$	$g_1^\circ=\sqrt{\frac{\kappa+\lambda+2\mu}{\rho}}$	$g_2^\circ=0$	$g_3^\circ=\sqrt{\frac{\kappa+2\mu}{2\rho}}$	$g_5^\circ=0$
$\lim_{k\to\infty}g_i(k)$	$g_1^\infty=\sqrt{\frac{\kappa+\lambda+2\mu}{\rho}}$	$g_2^\infty=\sqrt{\frac{\alpha+\beta+\gamma}{J\rho}}$	$g_3^\infty=\sqrt{\frac{\kappa+\mu}{\rho}}$	$g_5^\infty=\sqrt{\frac{\gamma}{J\rho}}$

2.2.1. Longitudinal waves

The eigenspace associated to the single eigenvalues $\omega_1^2(k)$ and $\omega_2^2(k)$ coincides with the line spanned by $\mathring{\mathbf{N}}\mathbf{v}_1$ with test vector $\mathbf{v}_1$. Depending on the associated eigenvectors $\boldsymbol{\varphi}_1(k)$ and $\boldsymbol{\varphi}_2(k)$, the wave solutions corresponding to each single eigenvalue can be classified on a proper physical–geometrical base

- The first eigenvalue ω_1^2 is associated with a real-valued eigenvector $\boldsymbol{\varphi}_1=(a\mathbf{n},\mathbf{0})$, corresponding to a wave propagating with no microrotations and displacements orthogonal to the wavefront. These waves can be termed *longitudinal displacement* waves. Their phase speed $c_1=\omega_1/k$ is independent of the wavenumber and systematically larger than the speed of the same class of waves propagating in the classical Cauchy continuum defined by the same constants λ and μ for the additional presence of the positive constant κ. The Cosserat medium is nondispersive for this class of waves, since the group speed $g_1=\partial\omega_1(k)/\partial k$ coincides with the phase speed c_1 and does not depend on the wavenumber.
- The second eigenvalue ω_2^2 is associated with a real-valued eigenvector $\boldsymbol{\varphi}_2=(\mathbf{0},b\mathbf{n})$, corresponding to a wave propagating with no displacements and microrotations about the axis orthogonal to the wavefront. These waves can be termed *longitudinal microrotation* waves. This class of waves is peculiar to the Cosserat continuum, since it is not supported by the classical Cauchy continuum. The Cosserat medium is dispersive for this class of waves, since the group speed $g_2(k)=c_2(k)+k\,\partial c_2(k)/\partial k$ depends on the wavenumber. Specifically, the group speed ranges between a null value $g_2^\circ=0$ in the limit of long wavelengths ($k\to 0$) and a finite value g_2^∞ in the limit of short wavelengths ($k\to\infty$). It is interesting to consider the expression of the eigenvalue $k_2^2(\omega)$ provided by the direct method. By introducing the auxiliary quantity $\omega_0^2=\kappa/(\rho J)$, the eigenvalue reads

$$k_2^2(\omega)=\frac{J\rho}{\Sigma}\left(\omega^2-2\omega_0^2\right), \tag{15}$$

  prompting the distinction of two different frequency ranges: (i) $\omega<\sqrt{2}\,\omega_0$ determines negative eigenvalues k_2^2 and imaginary-valued wavenumbers $k(\omega)$, corresponding to non-propagating waves, (ii) $\omega>\sqrt{2}\,\omega_0$ determines positive eigenvalues k_2^2 and real-valued wavenumbers $k(\omega)$, corresponding to propagating waves. Consequently, the *cutoff frequency* $\omega_c=\sqrt{2}\,\omega_0$ separates the low-frequency stopband from the high-frequency passband, in which longitudinal microrotation waves can propagate.

Qualitative diagrams of the frequencies $\omega_1(k)$ and $\omega_2(k)$, phase speeds $c_1(k)$ and $c_2(k)$, group speeds $g_{1,2}(k)$ and $g_2(k)$ over the real-valued positive k-domain are illustrated in Fig. 1. The related finite values in the limits of short and long wavelengths are reported in Table 1. Finally, waveforms described by normalized eigenvectors $\boldsymbol{\varphi}_1(k)$ and $\boldsymbol{\varphi}_2(k)$ are qualitatively illustrated in Fig. 2a,b.

2.2.2. Transverse waves

The eigenspace associated to the double eigenvalues $\omega_3^2(k)$ and $\omega_5^2(k)$ is the **n**-orthogonal plane, that is, the wavefront plane that is spanned by the vectors $(\mathbf{I}-\mathring{\mathbf{N}})\mathbf{v}_1$ and $\mathbf{N}\mathbf{v}_2$, with test vectors $\mathbf{v}_1$ and $\mathbf{v}_2$. The eigenvalue ω_3^2 is associated to a pair of complex-valued eigenvectors $\boldsymbol{\varphi}_3=(\boldsymbol{\varphi}_{a3},\boldsymbol{\varphi}_{b3})$ and $\boldsymbol{\varphi}_4=(\boldsymbol{\varphi}_{a4},\boldsymbol{\varphi}_{b4})$, satisfying relations $\boldsymbol{\varphi}_{b3}\cdot\mathbf{e}_2=0$ and $\boldsymbol{\varphi}_{b4}\cdot\mathbf{e}_3=0$, respectively. Similarly, eigenvalue ω_5^2 is associated to a pair of complex-valued eigenvectors $\boldsymbol{\varphi}_5=(\boldsymbol{\varphi}_{a5},\boldsymbol{\varphi}_{b5})$ and $\boldsymbol{\varphi}_6=(\boldsymbol{\varphi}_{a6},\boldsymbol{\varphi}_{b6})$, satisfying relations $\boldsymbol{\varphi}_{b5}\cdot\mathbf{e}_2=0$ and $\boldsymbol{\varphi}_{b6}\cdot\mathbf{e}_3=0$, respectively. Remarkably, the ith eigenvector ($i=3,\dots,6$) can also be normalized in the form $\boldsymbol{\varphi}_i=(\boldsymbol{\varphi}_{ai},I\boldsymbol{\varphi}_{bi})$ with real-valued subvectors $\boldsymbol{\varphi}_{ai},\boldsymbol{\varphi}_{bi}$ satisfying the relation $\boldsymbol{\varphi}_{ai}\cdot\boldsymbol{\varphi}_{bi}=0$. Consequently, the eigenvectors describe coupled waves propagating with both displacements and microrotations oscillating out-of-phase in the wavefront plane. These waves can be termed *transverse displacement–microrotation* waves, and cannot be encountered in the classical Cauchy continuum. An insightful physical classification of the waveform can be defined according to energetic criteria, by introducing the normalization-independent polarization factors

$$\begin{aligned}\Lambda_{ai}(k)&=\frac{\frac{1}{2}\omega_i^2(k)\,\mathbf{a}_i^\dagger(k)\left(\rho\mathbf{I}\right)\mathbf{a}_i(k)}{\frac{1}{2}\omega_i^2(k)\,\boldsymbol{\phi}_i^\dagger(k)\,\mathbf{M}\,\boldsymbol{\phi}_i(k)}=\frac{\boldsymbol{\varphi}_{ai}^\dagger(k)\,\boldsymbol{\varphi}_{ai}(k)}{\boldsymbol{\varphi}_i^\dagger(k)\,\boldsymbol{\varphi}_i(k)},\\ \Lambda_{bi}(k)&=\frac{\frac{1}{2}\omega_i^2(k)\,\mathbf{b}_i^\dagger(k)\left(\rho J\mathbf{I}\right)\mathbf{b}_i(k)}{\frac{1}{2}\omega_i^2(k)\,\boldsymbol{\phi}_i^\dagger(k)\,\mathbf{M}\,\boldsymbol{\phi}_i(k)}=\frac{\boldsymbol{\varphi}_{bi}^\dagger(k)\,\boldsymbol{\varphi}_{bi}(k)}{\boldsymbol{\varphi}_i^\dagger(k)\,\boldsymbol{\varphi}_i(k)},\end{aligned} \tag{16}$$

where dag indicate conjugate transpose.[1] Polarization factors $\Lambda_{ai}(k)$ and $\Lambda_{bi}(k)$ express the ratio of kinetic energy associated to the ith waveform $\boldsymbol{\varphi}_i$ that is stored in the subvectors $\boldsymbol{\varphi}_{ai}$ and $\boldsymbol{\varphi}_{bi}$, respectively [68–70]. By construction, the polarization factors can be recognized as secondary k-dependent (but **n**-independent) dispersion properties, related to each other by the complementary condition $\Lambda_{ai}+\Lambda_{bi}=1$. Polarization factors Λ_{ai} close to unity (and quasi-null Λ_{bi}) identify waves energetically dominated by eigendisplacements, which can be classified as *transverse displacement* waves. Differently, polarization factors Λ_{bi} close to unity (and quasi-null Λ_{ai}) identify waves energetically dominated by eigenrotations, which can be classified as *transverse microrotation* waves. It can be demonstrated that the eigenvector pairs associated to the same double eigenvalue have the same polarization factors (that is $\Lambda_{a3}=\Lambda_{a4}$ and $\Lambda_{a5}=\Lambda_{a6}$), and – remarkably – that the eigenvectors associated with different double eigenvalues have opposite polarizations (that is $\Lambda_{a3}=\Lambda_{b5}$ and $\Lambda_{b3}=\Lambda_{a5}$). The latter remark implies that two transverse displacement waves always coexist with two transverse microrotation waves for all parameter combinations in the whole wavenumber domain. Furthermore, it can be verified that the limits $\lim_{k\to 0}\Lambda_{a3}$ and $\lim_{k\to\infty}\Lambda_{a3}$ are coincident and unitary (and consequently $\lim_{k\to 0}\Lambda_{a5}=\lim_{k\to 0}(1-\Lambda_{b5})=\lim_{k\to 0}(1-\Lambda_{a3})$ and $\lim_{k\to\infty}\Lambda_{a5}=\lim_{k\to\infty}(1-\Lambda_{b5})=\lim_{k\to\infty}(1-\Lambda_{a3})$ are coincident and

[1] Note that here the polarization expresses a macroscopic property of the elastic waves, adapted from the theory of electro-magnetism and does not refer to the continuum micropolarity.

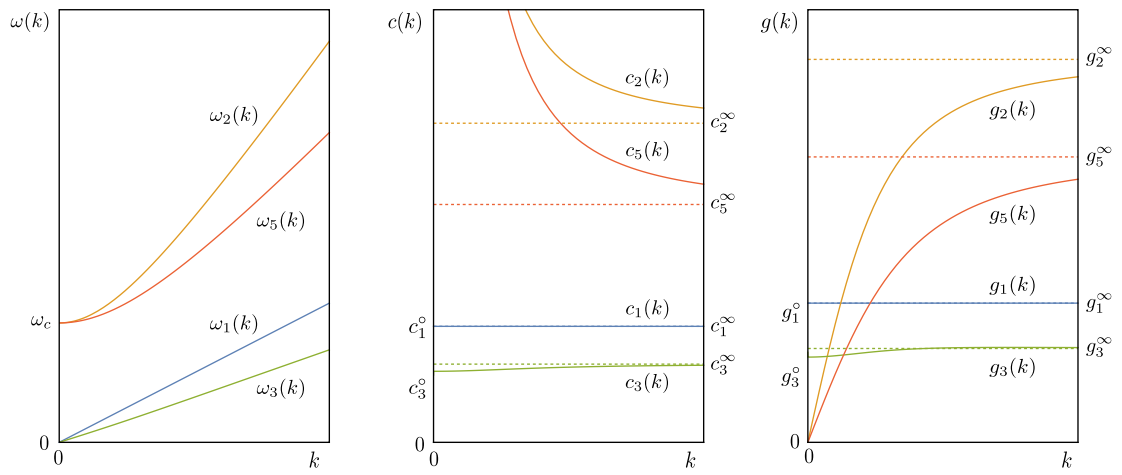

Fig. 1. Qualitative dispersion properties of the Cosserat continuum: frequency $\omega(k)$, phase speed $c(k)$, group speed $g(k)$. Dashed lines indicate finite values in the limit of short wavelengths ($k \to \infty$).

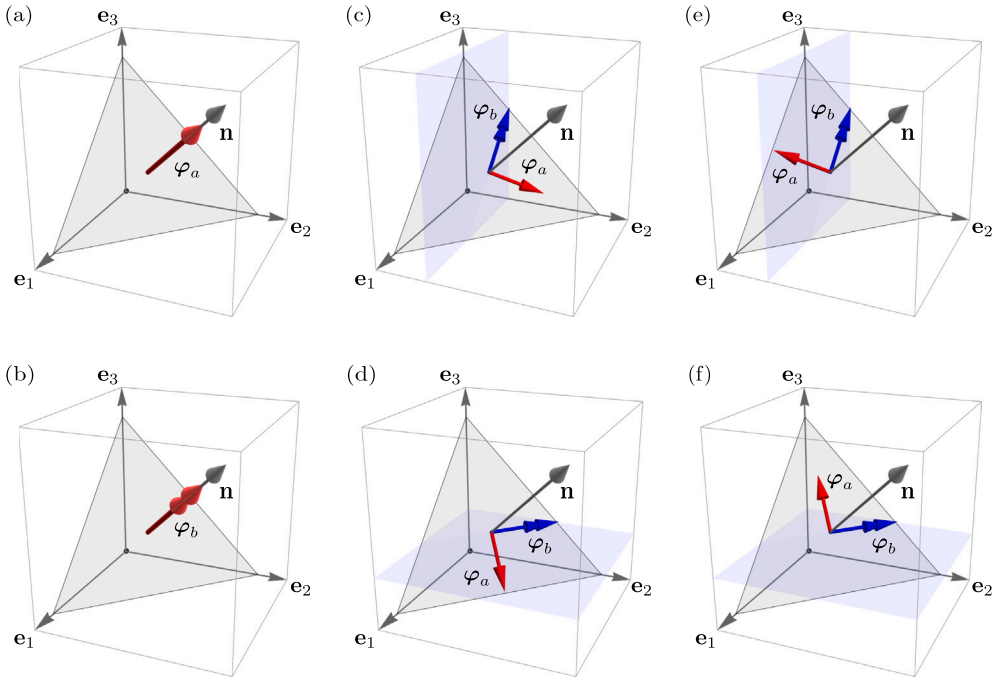

Fig. 2. Qualitative arrow-vector representation of the six normalized waveforms of plane harmonic waves that propagate in infinite micropolar continua: (a) *longitudinal displacement* waveform $\boldsymbol{\varphi}_1$, (b) *longitudinal microrotation* waveform $\boldsymbol{\varphi}_2$, (c),(d),(e),(f) *transverse displacement–microrotation* waveforms $\boldsymbol{\varphi}_3$, $\boldsymbol{\varphi}_4$, $\boldsymbol{\varphi}_5$, $\boldsymbol{\varphi}_6$. Single-arrow indicates subvector $\boldsymbol{\varphi}_a$ of eigendisplacements, double-arrow indicates subvector $\boldsymbol{\varphi}_{bi}$ of eigenrotations. Gray plane represents the $\mathbf{n}$-orthogonal wavefront. Red and blue colors indicate real-valued and imaginary-valued subvectors (lying in the blue planes), respectively.

null). As a primary physical consequence, the generic transverse wave is perfectly (and identically) polarized in both limits of long and short wavelengths. As a secondary physical consequence, a point of minimal polarization (that is, a minimum of $\Lambda_{a3}(k)$ or a maximum of $\Lambda_{a5}(k)$) must exist between the iso-polarized extremes of the k-domain. It can be demonstrated that this critical point is unique and systematically occurs at $k_p = \sqrt{2\kappa}/\sqrt{\gamma - J(\kappa+\mu)}$. The wavenumber k_p tends to fall in the range of long wavelengths (depending on the parameters κ, γ, μ, J) and may be physically relevant because it corresponds to the highest level of co-participation of displacements and microrotation in the waveform of transverse waves.

The Cosserat medium is dispersive for all transverse waves. Specifically, group velocity $g_3(k)$ ranges between the finite values g_3° and g_3^∞ (with $g_3^\infty > g_3^\circ$) in the limits of long and short wavelengths, respectively. Group velocity $g_5(k)$ ranges instead between zero and the finite value g_5^∞ in the limits of long and short wavelengths, respectively. It may be interesting to consider the alternative expression of the eigenvalue $k_5^2(\omega)$ provided by the direct method, reading

$$k_5^2(\omega) = \frac{\rho\Delta_2(\omega) - \rho\sqrt{\Delta_2^2(\omega) - 4\gamma J\omega^2(\kappa+\mu)\left(\omega^2 - 2\omega_0^2\right)}}{2\gamma(\kappa+\mu)}, \tag{17}$$

where $\Delta_2(\omega) = \left(\gamma\omega^2 + \kappa^2/\rho\right) + J(\kappa+\mu)\left(\omega^2 - 2\omega_0^2\right)$. Expression (17) allows distinction between: (i) the frequency range $\omega < \sqrt{2}\,\omega_0$ that gives negative eigenvalues k_5^2 and imaginary-valued wavenumbers $k(\omega)$, corresponding to non-propagating waves, (ii) the frequency range $\omega > \sqrt{2}\,\omega_0$ that gives positive eigenvalues k_5^2 and real-valued wavenumbers $k(\omega)$, corresponding to propagating waves. Therefore, similarly to the eigenvalue k_2^2, the *cutoff frequency* $\omega_c = \sqrt{2}\,\omega_0$ separates the low-frequency stopband from the high-frequency passband, in which transverse microrotation waves can propagate.

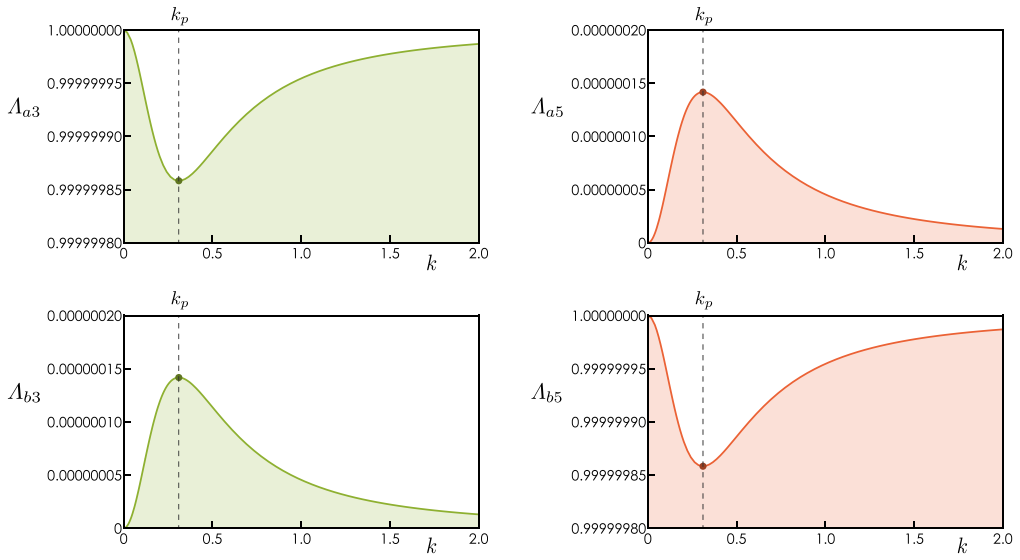

Fig. 3. Polarization factors Λ_{a3}, Λ_{b3}, Λ_{a5}, Λ_{b5} of transverse waves propagating with long wavelengths (range $k = [0, 2]$) in a Cosserat continuum characterized by parameter set $\boldsymbol{\mu}_\circ$, leading to critical wavenumber $k_p = 0.31061$.

Qualitative diagrams of the frequencies $\omega_3(k)$ and $\omega_5(k)$, phase speeds $c_3(k)$ and $c_5(k)$, group speeds $g_3(k)$ and $g_5(k)$ over the real-valued positive k-domain are illustrated in Fig. 1. The related finite values in the limits of short and long wavelengths are reported in Table 1. Waveforms described by normalized eigenvectors $\boldsymbol{\varphi}_{3,4}(k)$ and $\boldsymbol{\varphi}_{5,6}(k)$ are qualitatively illustrated in Fig. 2c,d,e,f. To exemplify, the polarization factors of the transverse waves are shown in Fig. 3 for a particular set $\boldsymbol{\mu}_\circ$ of elastic moduli and inertial parameters, which is aligned with the data proposed by [12] for Expanded Polystyrenes ($\alpha_\circ = \beta_\circ = \gamma_\circ = 168 * 10^4$ N, $\kappa_\circ = 51 * 10^3\,\mathrm{N/m^2}$, $\lambda_\circ = 444 * 10^5\,\mathrm{N/m^2}$, $\mu_\circ = 906 * 10^3\,\mathrm{N/m^2}$, $\rho_\circ = 32\,\mathrm{kg/m^3}$, $J_\circ = 4 * 10^{-1}\,\mathrm{m^4/m^2}$). Quasi-unitary polarization factors Λ_{a3} (equal to Λ_{a4}) and Λ_{b5} (equal to Λ_{a6}) reveal the transverse-displacement nature of waveforms φ_3 and φ_4 and the transverse-microrotation nature of waveforms φ_5 and φ_6, respectively.

3. Free wave propagation in micropolar plates

Differently from the synthetic approach adopted by the Kirchhoff–Love or Reissner–Mindlin theories, in which kinematics and dynamics of thin or thick plates are described by characteristic quantities related to the two-dimensional mid-plane, here the plate model is based on a full three-dimensional description. Specifically, the *micropolar plate* is intended as an unconstrained finite-thickness layer extracted from an infinite three-dimensional Cosserat continuum, confined between two parallel planes (Fig. 4a). For the sake of generality, no assumptions on plane strain conditions are introduced a priori. For convenience and without loss of generality, the origin of the Cartesian system is placed in the infinite mid-plane $\mathcal{M}$, identified by vectors $\mathbf{e}_1$ and $\mathbf{e}_2$ (in-plane directions) and spanned by coordinates x_1 and x_2. Consequently, the $\mathcal{M}$-orthogonal vector $\mathbf{e}_3$ (out-of-plane direction) is oriented along the finite thickness of the plate, denoted as height h and spanned by the coordinate x_3. The $\mathbf{e}_3$-orthogonal parallel planes play the role of *upper* ($x_3 = h/2$) and *lower* ($x_3 = -h/2$) free surfaces $\mathcal{S}_u$ and $\mathcal{S}_\ell$, respectively. The free wave propagation is governed by the equations of motion (9), equipped with free-stress and free-couple-stress boundary conditions, reading

$$\mathbf{Sn}_u = \mathbf{0}, \qquad \mathbf{Wn}_u = \mathbf{0}, \qquad \mathbf{Sn}_\ell = \mathbf{0}, \qquad \mathbf{Wn}_\ell = \mathbf{0}, \tag{18}$$

and applied to the upper and lower surfaces $\mathcal{S}_u$ (with $\mathbf{n}_u = \mathbf{e}_3$) and $\mathcal{S}_\ell$ (with $\mathbf{n}_\ell = -\mathbf{e}_3$). If dynamic excitation occurs at some point, the generated wave encounters the free surfaces several times during propagation, and mode conversion occurs [47]. After some reflections from the upper and lower surfaces, superpositions cause the emergence of "wave packets", commonly called *guided wavemodes*, which represent a characteristic dispersion property of the plate.

3.1. Partial wave technique

Among the different techniques available to determine the dispersion properties of guided waves in plates, the *partial wave technique* proposed by Solie and Auld [59] has the advantage of leading directly to wave solutions, thus providing insight in the physical nature of propagating waves [53]. According to this method, guided waves are expressed as the product between (i) a function defined across the thickness of the plate, properly referred to as the waveform, and (ii) a term that describes spatially-periodic propagation along the cross-section of the plate. By virtue of the isotropy, it can be assumed without loss of generality that no propagation occurs along coordinate x_2, hence wavenumber $k_2 = 0$. In the specific case of micropolar plates, the partial wave technique applies to both the displacement and the microrotation fields, which must be characterized by the same periodic propagation function

$$\begin{aligned} \mathbf{u}(\mathbf{x}_c, \mathbf{k}_c, \omega, t) &= \tilde{\mathbf{u}}\, \mathrm{e}^{I(\mathbf{k}_c \cdot \mathbf{x}_c - \omega t)}, \\ \boldsymbol{\theta}(\mathbf{x}_c, \mathbf{k}_c, \omega, t) &= \tilde{\boldsymbol{\theta}}\, \mathrm{e}^{I(\mathbf{k}_c \cdot \mathbf{x}_c - \omega t)}, \end{aligned} \tag{19}$$

where $\tilde{\mathbf{u}} = (\tilde{u}_1, \tilde{u}_2, \tilde{u}_3)^\top$ and $\tilde{\boldsymbol{\theta}} = (\tilde{\theta}_1, \tilde{\theta}_2, \tilde{\theta}_3)^\top$ are amplitude vectors. Tentative solutions (19) describe a progressive displacement–microrotation wave that harmonically oscillates in time with frequency ω while periodically propagating in the space spanned by coordinate vector $\mathbf{x}_c = (x_1, 0, x_3)^\top$ along the direction of wavevector $\mathbf{k}_c = (k_1, 0, k_3)^\top$. During propagation, the wave is reflected back and forth between the upper and lower surfaces of the plate, as long as the inclination angle $\chi = \arctan(k_3/k_1)$ differs from zero. Consequently, the propagation function can be conveniently re-parameterized as

$$\begin{aligned} \mathbf{u}(\mathbf{x}_c, k_1, \phi, \omega, t) &= \tilde{\mathbf{u}}\, \mathrm{e}^{I(k_1(x_1 + \phi x_3) - \omega t)}, \\ \boldsymbol{\theta}(\mathbf{x}_c, k_1, \phi, \omega, t) &= \tilde{\boldsymbol{\theta}}\, \mathrm{e}^{I(k_1(x_1 + \phi x_3) - \omega t)}, \end{aligned} \tag{20}$$

where the inclination parameter $\phi = k_3/k_1 = \tan\chi$ replaces the wavenumber k_3 in the parametric determination of the direct dispersion relation $\omega(\mathbf{k})$ for guided waves. It is worth noting that the introduction of the parameter ϕ is equivalent to enforce a constraint between the wavenumbers k_3 and k_1, which excludes the possibility to describe

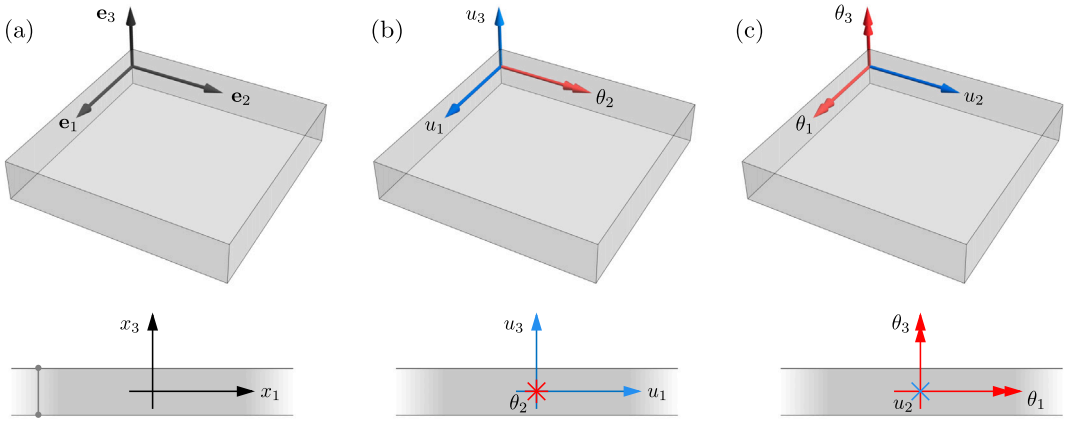

Fig. 4. Micropolar plate: (a) coordinate system and cross-section; (b) variables of the *in-plane* guided wave problem; (c) variables of the *off-plane* guided wave problem.

through-thickness wave propagation. This kind of waves propagates in a wavefrequency range higher than guided waves [71].

By substituting the tentative solution (20) into the homogeneous equations of motion (9) an algebraic eigenproblem is obtained. Specifically, it is convenient to express the unknown waveforms as $\tilde{\mathbf{u}} = \mathbf{B}_{up}\tilde{\mathbf{p}} + \mathbf{B}_{uq}\tilde{\mathbf{q}}$ and $\tilde{\theta} = \mathbf{B}_{\theta p}\tilde{\mathbf{p}} + \mathbf{B}_{\theta q}\tilde{\mathbf{q}}$, by defining the sub-waveforms $\tilde{\mathbf{p}} = (\tilde{u}_1, \tilde{u}_3, \tilde{\theta}_2)^\top$ and $\tilde{\mathbf{q}} = (\tilde{u}_2, \tilde{\theta}_1, \tilde{\theta}_3)^\top$ and introducing three-by-three boolean matrices $\mathbf{B}_{up}$, $\mathbf{B}_{uq}$, $\mathbf{B}_{\theta p}$, $\mathbf{B}_{\theta q}$, reported in Appendix. Accordingly, the eigenproblem can be decomposed in the form

$$\begin{bmatrix} \mathbf{K}_p(\phi, k_1) - \omega^2 \mathbf{M}_p & \mathbf{O} \\ \mathbf{O} & \mathbf{K}_q(\phi, k_1) - \omega^2 \mathbf{M}_q \end{bmatrix} \begin{pmatrix} \tilde{\mathbf{p}} \\ \tilde{\mathbf{q}} \end{pmatrix} = \begin{pmatrix} \mathbf{0} \\ \mathbf{0} \end{pmatrix}, \tag{21}$$

where the equivalent stiffness submatrices are Hermitian. Specifically, by introducing the auxiliary quantities $K_1 = \kappa + \lambda + 2\mu$ and $K_2 = \kappa + \mu$, the stiffness submatrices read

$$\mathbf{K}_p(\phi, k_1) = \begin{bmatrix} k_1^2(K_1 + K_2\phi^2) & k_1^2(\lambda+\mu)\phi & Ik_1\kappa\phi \\ k_1^2(\lambda+\mu)\phi & k_1^2(K_2 + K_1\phi^2) & -Ik_1\kappa \\ -Ik_1\kappa\phi & Ik_1\kappa & 2\kappa + k_1^2\gamma(1+\phi^2) \end{bmatrix}, \tag{22}$$

$$\mathbf{K}_q(\phi, k_1) = \begin{bmatrix} k_1^2 K_2(1+\phi^2) & -Ik_1\kappa\phi & Ik_1\kappa \\ Ik_1\kappa\phi & 2\kappa + k_1^2(\Sigma + \gamma\phi^2) & k_1^2(\alpha+\beta)\phi \\ -Ik_1\kappa & k_1^2(\alpha+\beta)\phi & 2\kappa + k_1^2(\gamma + \Sigma\phi^2) \end{bmatrix}, \tag{23}$$

while the mass submatrices are $\mathbf{M}_p = \mathrm{diag}(\rho, \rho, J\rho)$ and $\mathbf{M}_q = \mathrm{diag}(\rho, J\rho, J\rho)$. The decomposition (21) highlights the possibility of distinguishing two uncoupled sub-eigenproblems. The former sub-eigenproblem, governed by the matrices $\mathbf{K}_p(\phi, k_1)$ and $\mathbf{M}_p$, rules the guided waves characterizing the *in-plane* motion of the plate cross-section, described by the eigencomponents of sub-waveform $\tilde{\mathbf{p}}$ (two displacements and one microrotation, see Fig. 4b). It is worth remarking that the in-plane sub-eigenproblem depends on the constitutive parameters γ, κ, λ, μ only (while it is independent of α and β). The latter sub-eigenproblem, governed by the matrices $\mathbf{K}_q(\phi, k_1)$ and $\mathbf{M}_q$, rules the guided waves characterizing the *off-plane* motion of the plate cross-section, described by the eigencomponents of sub-waveform $\tilde{\mathbf{q}}$ (one displacement and two microrotations, see Fig. 4c). It is worth remarking that the off-plane sub-eigenproblem depends on the constitutive parameters α, β, γ, κ, μ only (while it is independent of parameter λ).

The partial wave technique adopts the inclination parameter ϕ as the primary unknown, to be determined first in the dispersion relation. Therefore, considering the frequency ω and the wavenumber k_1 as parameters, Eqs. (21) define a parametric eigenproblem where ϕ plays the role of eigenvalue. Considering first the sub-eigenproblem $\big(\mathbf{K}_p(\phi, k_1) - \omega^2\mathbf{M}_p\big)\tilde{\mathbf{p}} = \mathbf{0}$ governing the in-plane problem, the characteristic equation provides three solutions for the unknown $\phi^2(\omega, k_1)$. Each solution $\phi_p^2(\omega, k_1)$ corresponds to a pair of eigenvalues $\phi_{pj}^+(\omega, k_1)$ and $\phi_{pj}^-(\omega, k_1)$ and two three-by-one eigenvectors $\boldsymbol{\varphi}_{pj}^+(\omega, k_1)$ and $\boldsymbol{\varphi}_{pj}^-(\omega, k_1)$, with $j = 1, \dots, 3$. Clearly, the eigenvalues are opposite to each other $\phi_{pj}^- = -\phi_{pj}^+$, while the eigenvectors satisfy the relevant condition $\boldsymbol{\varphi}_{pj}^+ + \boldsymbol{\varphi}_{pj}^- = (1, 0, 0)^\top$, if appropriately normalized. Similarly, the sub-eigenproblem $\big(\mathbf{K}_q(\phi, k_1) - \omega^2\mathbf{M}_q\big)\tilde{\mathbf{q}} = \mathbf{0}$, governing the off-plane problem, provides three solutions for the unknown $\phi^2(\omega, k_1)$, which generally differ from those of the other eigenproblem. Each solution $\phi_q^2(\omega, k_1)$ corresponds to a pair of eigenvalues $\phi_{qj}^+(\omega, k_1)$ and $\phi_{qj}^-(\omega, k_1)$ and two three-by-one eigenvectors $\boldsymbol{\varphi}_{qj}^+(\omega, k_1)$ and $\boldsymbol{\varphi}_{qj}^-(\omega, k_1)$ with $j = 1, \dots, 3$. The eigenvalues are opposite to each other $\phi_{qj}^- = -\phi_{qj}^+$, while the eigenvectors satisfy the relevant condition $\boldsymbol{\varphi}_{qj}^+ + \boldsymbol{\varphi}_{qj}^- = (0, 1, 0)^\top$, if appropriately normalized.

After normalization, the triads of eigenvectors $\boldsymbol{\varphi}_{pj}^+(\omega, k_1)$ and $\boldsymbol{\varphi}_{pj}^-(\omega, k_1)$ can be collected column-wise in the three-by-three eigenmatrices $\boldsymbol{\Psi}_p^+(\omega, k_1)$ and $\boldsymbol{\Psi}_p^-(\omega, k_1)$ or in the three-by-six eigenmatrix $\boldsymbol{\Psi}_p(\omega, k_1) = \big[\boldsymbol{\Psi}_p^+(\omega, k_1), \boldsymbol{\Psi}_p^-(\omega, k_1)\big]$. Similarly, the triads of eigenvectors $\boldsymbol{\varphi}_{qj}^+(\omega, k_1)$ and $\boldsymbol{\varphi}_{qj}^-(\omega, k_1)$ can be collected column-wise in the three-by-three eigenmatrices $\boldsymbol{\Psi}_q^+(\omega, k_1)$ and $\boldsymbol{\Psi}_q^-(\omega, k_1)$ or in the three-by-six eigenmatrix $\boldsymbol{\Psi}_q(\omega, k_1) = \big[\boldsymbol{\Psi}_q^+(\omega, k_1), \boldsymbol{\Psi}_q^-(\omega, k_1)\big]$. Due to the completeness of the eigenspace, the guided harmonic wave propagating periodically through the plate can be expressed by linear superposition of all the eigenvectors. For the in-plane problem, the superposition reads

$$\begin{aligned} \mathbf{u}_p(\mathbf{x}_c, k_1, \omega, t) &= \mathbf{B}_{up}\boldsymbol{\Psi}_p(\omega, k_1)\,\mathbf{E}_p(\mathbf{x}_c, \omega, k_1, t)\,\mathbf{c}_p, \\ \theta_p(\mathbf{x}_c, k_1, \omega, t) &= \mathbf{B}_{\theta p}\boldsymbol{\Psi}_p(\omega, k_1)\,\mathbf{E}_p(\mathbf{x}_c, \omega, k_1, t)\,\mathbf{c}_p, \end{aligned} \tag{24}$$

where the six-by-six exponential matrix $\mathbf{E}_p(\mathbf{x}_c, \omega, k_1, t) = \exp\big[I\big(\mathbf{I}k_1(\mathbf{I}x_1 + \boldsymbol{\Phi}_p(\omega, k_1)x_3) - \mathbf{I}\omega t\big)\big]$ depends on the six-by-six diagonal matrices $\boldsymbol{\Phi}_p = \mathrm{diag}(\phi_{p1}^+, \phi_{p2}^+, \phi_{p3}^+, \phi_{p1}^-, \phi_{p2}^-, \phi_{p3}^-)$, while $\mathbf{c}_p$ is the six-by-one vector of combination coefficients. For the off-plane problem, the superposition is

$$\begin{aligned} \mathbf{u}_q(\mathbf{x}_c, k_1, \omega, t) &= \mathbf{B}_{uq}\boldsymbol{\Psi}_q(\omega, k_1)\mathbf{E}_q(\mathbf{x}_c, \omega, k_1, t)\mathbf{c}_q, \\ \theta_q(\mathbf{x}_c, k_1, \omega, t) &= \mathbf{B}_{\theta q}\boldsymbol{\Psi}_q(\omega, k_1)\mathbf{E}_q(\mathbf{x}_c, \omega, k_1, t)\mathbf{c}_q, \end{aligned} \tag{25}$$

where the six-by-six exponential matrix $\mathbf{E}_q(\mathbf{x}_c, \omega, k_1, t) = \exp\big[I\big(\mathbf{I}k_1(\mathbf{I}x_1 + \boldsymbol{\Phi}_q(\omega, k_1)x_3) - \mathbf{I}\omega t\big)\big]$ depends on the six-by-six diagonal matrix $\boldsymbol{\Phi}_q = \mathrm{diag}(\phi_{q1}^+, \phi_{q2}^+, \phi_{q3}^+, \phi_{q1}^-, \phi_{q2}^-, \phi_{q3}^-)$, while $\mathbf{c}_q$ is the six-by-one vector of combination coefficients.

3.1.1. In-plane problem

Considering first the in-plane problem, the displacement-microrotation field described by the harmonic waves (24) is found to determine a plane state of strain and microcurvature. Specifically, by recalling the kinematic relations (3) and applying some differential

algebra, the tensors of strain and microcurvature can be expressed as

$$\boldsymbol{\epsilon}_p(\mathbf{x}_c,\omega,k_1,t) = \mathbf{B}_{up}\boldsymbol{\Psi}_p(\omega,k_1)\big[\mathbf{c}_p\cdot\mathbb{E}_p(\mathbf{x}_c,\omega,k_1,t)\big]+ - \big[(\mathbf{B}_{\theta p}\boldsymbol{\Psi}_p(\omega,k_1)\mathbf{E}_p(\mathbf{x}_c,\omega,k_1,t)\mathbf{c}_p)\times\mathbf{e}_i\big]\otimes\mathbf{e}_i, \tag{26}$$

$$\boldsymbol{\kappa}_p(\mathbf{x}_c,\omega,k_1,t) = \mathbf{B}_{\theta p}\boldsymbol{\Psi}_p(\omega,k_1)\big[\mathbf{c}_p\cdot\mathbb{E}_p(\mathbf{x}_c,\omega,k_1,t)\big], \tag{27}$$

where summation is understood for the repeated index i, according to the Einstein notation, while $\mathbb{E}_p(\mathbf{x}_c,\omega,k_1,t) = \nabla\big(\mathbf{E}_p^{\top}(\mathbf{x}_c,\omega,k_1,t)\big)$ is a six-by-six-by-three tensor of third order. It is worth noting that the activated (not null) strains are ϵ_{11}, ϵ_{13}, ϵ_{31} and ϵ_{33}, while the activated microcurvatures are κ_{21} and κ_{23}. Therefore, by applying the elastic constitutive equations (7), the corresponding state of stress and microcouple stress can be expressed by the tensors

$$\mathbf{S}_p(\mathbf{x}_c,\omega,k_1,t) = 2\mu\boldsymbol{\epsilon}_p^{\mathrm{S}}(\mathbf{x}_c,\omega,k_1,t)+ + \lambda\big[\operatorname{tr}\boldsymbol{\epsilon}_p(\mathbf{x}_c,\omega,k_1,t)\big]\mathbf{I}+\kappa\boldsymbol{\epsilon}_p(\mathbf{x}_c,\omega,k_1,t), \tag{28}$$

$$\mathbf{W}_p(\mathbf{x}_c,\omega,k_1,t) = \alpha\big[\operatorname{tr}\boldsymbol{\kappa}_p(\mathbf{x}_c,\omega,k_1,t)\big]\mathbf{I}+ + \beta\boldsymbol{\kappa}_p^{\top}(\mathbf{x}_c,\omega,k_1,t)+\gamma\boldsymbol{\kappa}_p(\mathbf{x}_c,\omega,k_1,t), \tag{29}$$

where $\boldsymbol{\epsilon}_p^{\mathrm{S}}(\mathbf{x}_c,\omega,k_1,t) = \operatorname{sym}\big(\boldsymbol{\epsilon}_p(\mathbf{x}_c,\omega,k_1,t)\big)$. It is worth noting that the activated stresses are $S_{11}, S_{13}, S_{22}, S_{31}$ and S_{33}, while the activated microcouples are W_{12}, W_{21}, W_{23} and W_{32}.

Once the state of stress and microcouple is known for the generic position vector $\mathbf{x}_c$ of the plate, the boundary conditions (18) can be enforced by specifying the position vectors $\mathbf{x}_u = (x_1,0,h/2)$ and $\mathbf{x}_\ell = (x_1,0,-h/2)$ for the upper and lower surfaces $\mathcal{S}_u$ and $\mathcal{S}_\ell$, respectively. By virtue of the problem linearity and the possibility of factoring out the exponential term $\mathbf{E}_1(x_1,\omega,k_1,t) = \exp\big[I(k_1x_1-\omega t)\mathbf{I}\big]$, the full set of conditions $\mathbf{S}_p(\mathbf{x}_u,\omega,k_1,t)\mathbf{e}_3 = \mathbf{0}$, $\mathbf{W}_p(\mathbf{x}_u,\omega,k_1,t)\mathbf{e}_3 = \mathbf{0}$ (for $\mathcal{S}_u$) and $-\mathbf{S}_p(\mathbf{x}_\ell,\omega,k_1,t)\mathbf{e}_3 = \mathbf{0}$, $-\mathbf{W}_p(\mathbf{x}_\ell,\omega,k_1,t)\mathbf{e}_3 = \mathbf{0}$ (for $\mathcal{S}_\ell$) can be expressed in the form

$$\mathbf{C}_p(\omega,k_1)\mathbf{c}_p = \mathbf{0}, \tag{30}$$

where $\mathbf{C}_p(\omega,k_1)$ is a six-by-six matrix, once the six self-satisfied boundary conditions related to inactive stresses and microcouples are eliminated. Eq. (30) states a new algebraic eigenproblem. Indeed, by assigning the real-valued frequency ω as free parameter and the real-valued wavenumber k_1 as unknown eigenvalue, zeroing the characteristic function $F_p(\omega,k_1) = \det\mathbf{C}_p(\omega,k_1)$, the direct dispersion relation $k_1(\omega)$ can be determined. As an alternative, by reversing the roles of frequency and wavenumber, the inverse dispersion relation $\omega(k_1)$ can be obtained. Each single eigenvalue $\omega_i(k_1)$ corresponds to a not-trivial complex-valued solution $\mathbf{c}_{pi}(k_1)$, playing the role of eigenvector with undetermined amplitude. Each eigenpair $(\omega_i(k_1),\mathbf{c}_{pi}(k_1))$ specifies the displacement and microrotation fields $\mathbf{u}_{pi}(\mathbf{x}_c,k_1,t)$ and $\boldsymbol{\theta}_{pi}(\mathbf{x}_c,k_1,t)$ of the guided wave oscillating harmonically with frequency $\omega_i(k_1)$ and propagating periodically in the direction of the wavevector $\mathbf{k}_1 = (k_1,0,0)^{\top}$. Assuming unitary amplitude, the fields have the expression

$$\begin{aligned}\mathbf{u}_{pi}(\mathbf{x}_c,k_1,t) &= \mathbf{B}_{up}\boldsymbol{\psi}_{pi}(x_3,k_1)\,\mathrm{e}^{I[k_1x_1-\omega_i(k_1)t]},\\ \boldsymbol{\theta}_{pi}(\mathbf{x}_c,k_1,t) &= \mathbf{B}_{\theta p}\boldsymbol{\psi}_{pi}(x_3,k_1)\,\mathrm{e}^{I[k_1x_1-\omega_i(k_1)t]},\end{aligned} \tag{31}$$

where $\boldsymbol{\psi}_{pi}(x_3,k_1) = \boldsymbol{\Psi}_p(\omega_i(k_1),k_1)\mathbf{E}_{pi}(x_3,k_1)\mathbf{c}_{pi}(k_1) = (v_{1i}(x_3,k_1), v_{3i}(x_3,k_1),\vartheta_{2i}(x_3,k_1))^{\top}$ is the three-by-one vector collecting the non-propagating x_3-dependent waveforms, or *standing wavemodes*, of the in-plane motion components (displacements u_1 and u_3 and rotation θ_2), whose shapes in the domain $\mathcal{X}_3 = \{x_3 : -h/2 \le x_3 \le h/2\}$ are governed by the six-by-six exponential matrix $\mathbf{E}_{pi}(x_3,k_1) = \exp\big[I\boldsymbol{\Phi}_p(\omega_i(k_1),k_1)x_3\big]$. From the physical viewpoint, the in-plane guided waves (31) can be interpreted as longitudinal- or flexural-type motions accompanied by a microrotation field. In the limiting case of vanishing micropolar parameters, these motions recover the Rayleigh–Lamb waves of the classical Cauchy continuum.

3.1.2. Off-plane problem

Considering the off-plane problem, the displacement–microrotation field described by the harmonic waves (25) is found to determine a plane state of strain and microcurvature. The tensors of strain and microcurvature have an expression that is formally similar to that of the in-plane problem

$$\boldsymbol{\epsilon}_q(\mathbf{x}_c,\omega,k_1,t) = \mathbf{B}_{uq}\boldsymbol{\Psi}_q(\omega,k_1)\big[\mathbf{c}_q\cdot\mathbb{E}_q(\mathbf{x}_c,\omega,k_1,t)\big]+ - \big[(\mathbf{B}_{\theta q}\boldsymbol{\Psi}_q(\omega,k_1)\mathbf{E}_q(\mathbf{x}_c,\omega,k_1,t)\mathbf{c}_q)\times\mathbf{e}_i\big]\otimes\mathbf{e}_i, \tag{32}$$

$$\boldsymbol{\kappa}_q(\mathbf{x}_c,\omega,k_1,t) = \mathbf{B}_{\theta q}\boldsymbol{\Psi}_q(\omega,k_1)\big[\mathbf{c}_q\cdot\mathbb{E}_q(\mathbf{x}_c,\omega,k_1,t)\big], \tag{33}$$

where summation is understood for the repeated index i, while $\mathbb{E}_q(\mathbf{x}_c,\omega,k_1,t) = \nabla\big(\mathbf{E}_q^{\top}(\mathbf{x}_c,\omega,k_1,t)\big)$ is a six-by-six-by-three tensor of third order. Complementarily to the in-plane problem, the activated (not null) strains are ϵ_{12}, ϵ_{21}, ϵ_{23} and ϵ_{32}, while the activated microcurvatures are κ_{11}, κ_{13}, κ_{31} and κ_{33}. Therefore, by applying the elastic constitutive equations (7), the corresponding state of stress and microcouple can be expressed by the tensors

$$\mathbf{S}_q(\mathbf{x}_c,\omega,k_1,t) = 2\mu\,\boldsymbol{\epsilon}_q^{\mathrm{S}}(\mathbf{x}_c,\omega,k_1,t)+ + \lambda\big[\operatorname{tr}\boldsymbol{\epsilon}_q(\mathbf{x}_c,\omega,k_1,t)\big]\mathbf{I}+\kappa\,\boldsymbol{\epsilon}_q(\mathbf{x}_c,\omega,k_1,t), \tag{34}$$

$$\mathbf{W}_q(\mathbf{x}_c,\omega,k_1,t) = \alpha\big[\operatorname{tr}\boldsymbol{\kappa}_q(\mathbf{x}_c,\omega,k_1,t)\big]\mathbf{I}+ + \beta\,\boldsymbol{\kappa}_q^{\top}(\mathbf{x}_c,\omega,k_1,t)+\gamma\,\boldsymbol{\kappa}_q(\mathbf{x}_c,\omega,k_1,t), \tag{35}$$

where $\boldsymbol{\epsilon}_q^{\mathrm{S}}(\mathbf{x}_c,\omega,k_1,t) = \operatorname{sym}\big(\boldsymbol{\epsilon}_q(\mathbf{x}_c,\omega,k_1,t)\big)$. Complementarily to the in-plane problem, the activated stresses are S_{12}, S_{21}, S_{23} and S_{32}, while the activated microcouples are W_{11}, W_{13}, W_{31}, W_{22} and W_{33}.

Once the state of stress and microcouple is known for the generic position vector $\mathbf{x}_c$ of the plate, the boundary conditions (18) can be imposed by specifying the position vectors $\mathbf{x}_u = (x_1,0,h/2)$ and $\mathbf{x}_\ell = (x_1,0,-h/2)$ for the upper and lower surfaces $\mathcal{S}_u$ and $\mathcal{S}_\ell$, respectively. By virtue of the problem linearity and the possibility of factoring out the exponential term $\mathbf{E}_1(x_1,\omega,k_1,t) = \exp\big[I(k_1x_1-\omega t)\mathbf{I}\big]$, the full set of conditions $\mathbf{S}_q(\mathbf{x}_u,\omega,k_1,t)\mathbf{e}_3 = \mathbf{0}$, $\mathbf{W}_q(\mathbf{x}_u,\omega,k_1,t)\mathbf{e}_3 = \mathbf{0}$ (for $\mathcal{S}_u$) and $-\mathbf{S}_q(\mathbf{x}_\ell,\omega,k_1,t)\mathbf{e}_3 = \mathbf{0}$, $-\mathbf{W}_q(\mathbf{x}_\ell,\omega,k_1,t)\mathbf{e}_3 = \mathbf{0}$ (for $\mathcal{S}_\ell$) can be expressed in the form

$$\mathbf{C}_q(\omega,k_1)\mathbf{c}_q = \mathbf{0}, \tag{36}$$

where $\mathbf{C}_q(\omega,k_1)$ is a six-by-six matrix, having eliminated the six self-satisfied boundary conditions related to inactive stresses and microcouples. Eq. (36) states a new algebraic eigenproblem. Indeed, by assigning the real-valued frequency ω as free parameter and the real-valued wavenumber k_1 as unknown eigenvalue, zeroing the characteristic function $F_q(\omega,k_1) = \det\mathbf{C}_q(\omega,k_1)$, the direct dispersion relation $k_1(\omega)$ can be determined. As an alternative, by reversing the roles of frequency and wavenumber, the inverse dispersion relation $\omega(k_1)$ can be obtained. Each single eigenvalue $\omega_i(k_1)$ corresponds to a non-trivial complex-valued solution $\mathbf{c}_{qi}(k_1)$, playing the role of eigenvector with undetermined amplitude. Each eigenpair $(\omega_i(k_1),\mathbf{c}_{qi}(k_1))$ specifies the displacement and microrotation fields $\mathbf{u}_{qi}(\mathbf{x}_c,k_1,t)$ and $\boldsymbol{\theta}_{qi}(\mathbf{x}_c,k_1,t)$ of the guided wave oscillating harmonically with frequency $\omega_i(k_1)$ and propagating periodically in the direction of the wavevector $\mathbf{k}_1 = (k_1,0,0)^{\top}$. Assuming unitary amplitude, the fields have the expression

$$\begin{aligned}\mathbf{u}_{qi}(\mathbf{x}_c,k_1,t) &= \mathbf{B}_{uq}\boldsymbol{\psi}_{qi}(x_3,k_1)\,\mathrm{e}^{I[k_1x_1-\omega_i(k_1)t]},\\ \boldsymbol{\theta}_{qi}(\mathbf{x}_c,k_1,t) &= \mathbf{B}_{\theta q}\boldsymbol{\psi}_{qi}(x_3,k_1)\,\mathrm{e}^{I[k_1x_1-\omega_i(k_1)t]},\end{aligned} \tag{37}$$

where $\boldsymbol{\psi}_{qi}(x_3,k_1) = \boldsymbol{\Psi}_q(\omega_i(k_1),k_1)\mathbf{E}_{qi}(x_3,k_1)\mathbf{c}_{qi}(k_1) = (v_{2i}(x_3,k_1), \vartheta_{1i}(x_3,k_1),\vartheta_{3i}(x_3,k_1))^{\top}$ is the three-by-one vector collecting the non-propagating x_3-dependent waveforms, or *standing wavemodes*, of the off-plane motion components (displacement u_2 and rotations θ_1 and θ_3), whose shapes in the domain $\mathcal{X}_3 = \{x_3 : -h/2 \le x_3 \le h/2\}$ are governed by the six-by-six exponential matrix $\mathbf{E}_{qi}(x_3,k_1) = \exp\big[I\boldsymbol{\Phi}_q(\omega_i(k_1),k_1)x_3\big]$. From the physical viewpoint, the off-plane guided waves (37) can be interpreted as shear-type waves associated with microrotation fields acting in the plane orthogonal to the propagation direction. These transverse displacement–microrotation motions represent the micropolar analogue of the SH waves in a Cauchy continuum.

4. In-plane guided waves

Since the in-plane and off-plane problems are uncoupled and governed by formally similar equations, the investigation and discussion of their solutions can be limited to the in-plane problem. By assuming the real-valued wavenumber k_1 as independent variable, the direct dispersion relations for the wavefrequency $\omega_p(k_1)$ and the standing wavemodes $\boldsymbol{\psi}_p(x_3, k_1)$ characterize the free propagation of in-plane guided waves for the micropolar plate. Furthermore, the phase speed $c_p(k_1) = \omega_p(k_1)/k_1$ and the group speed $g_p(k_1) = \partial\omega_p(k_1)/\partial k_1$ represent secondary dispersion properties of major interest from the physical point of view.

4.1. Dispersion diagrams

The relation $\omega_p(k_1)$ describes the dispersion diagram in the wavenumber–wavefrequency plane. Since the mathematical relation $\omega_p(k_1)$ is generally multi-valued (depending on the number and multiplicity of the roots of the characteristic function $F_p(\omega, k_1)$ for a given wavenumber), the dispersion diagram is multi-branched, with different branches corresponding to distinct dispersion curves. As long as the dispersion curves possess a certain geometric continuity, the ith branch of the dispersion diagrams for the in-plane problem can be constructed by numerically tracking the ith solution $\omega_{pi}(k_1)$ of the characteristic equation $F_p(\omega, k_1) = 0$ under variation of the wavenumber k_1. The complete set of solutions is referred to as the dispersion spectrum. Once the ith solution $\omega_{pi}(k_1)$ is known, the corresponding phase speed $c_{pi}(k_1)$ and group speed $g_{pi}(k_1)$ can be determined numerically, while the wavemode $\boldsymbol{\psi}_{pi}(x_3, k_1)$ is analytically associated to each pair $(k_1, \omega_{pi}(k_1))$. Therefore, the eigensolution must be considered semi-analytical in the general case.

The dispersion diagrams for the micropolar plate characterized by thickness $h_\circ = 5 * 10^{-3}$ m and the particular set $\boldsymbol{\mu}_\circ$ of constitutive parameters are considered. Specifically, the dispersion branches of the ten frequencies $\omega_{p1}(k_1), \dots, \omega_{p10}(k_1)$ associated to the lowest phase speeds $c_{p1}(k_1), \dots, c_{p10}(k_1)$ are reported in Fig. 5. According to the traditional representation (see for instance the textbooks [53,54]), the diagrams of phase speed c_p and group speed g_p are illustrated versus positive real-valued circular frequencies ω or products fh, where the frequency $f = \omega/(2\pi)$. Since a major interest is in the constitutive coupling between displacement and micro-rotation fields, the reference case with lower coupling ($\kappa = 51 * 10^3$ N/m^2, see Figs. 5a,b) is compared with the case with higher coupling ($\kappa = 51 * 10^4$ N/m^2, see Figs. 5c,d). Independently of the constitutive coupling, a strong density of dispersion branches occurs in the investigated range. As primary remark, the strong differences between the phase and group speeds confirm the dispersive nature of the micropolar continuum for guided waves. Qualitatively, all the dispersion curves tend to reach finite limit values of phase and group speeds for very high frequencies. The majority of dispersion curves is also characterized by cutoff frequencies, corresponding to the lowest attainable real ω-values (identifiable as vertical asymptotes in Figs. 5a,c). The curve intersections that occur in the phase speed dispersion diagram correspond to pairs of identical frequencies (for the same wavenumber), giving rise to *resonance* conditions. Note that intersections in the dispersion diagram of the group speed do not correspond to resonances in the general case. Local phenomena generated by resonances are discussed in Section 4.3.

By adopting the classical codification of Rayleigh–Lamb waves, the S-family of dispersion curves corresponding to *Symmetric waves* (red curves) can be distinguished from the A-family of dispersion curves corresponding to *Antisymmetric waves* (blue curves). The geometric criterion for one or the other classification depends on the morphology of the wavemode $\boldsymbol{\psi}_{pi}(x_3, k_1)$ that characterizes each curve. Given that the wavemodes $\boldsymbol{\psi}_{pi}(x_3, k_1)$ are dominated by the modal displacements υ_1 and υ_3, while negligibly participated by the modal microrotation ϑ_2, symmetry and antisymmetry refer to the $\mathbf{k}_1$-aligned modal function $\upsilon_1(x_3)$ in the domain $\mathcal{X}_3$. By sorting the dispersion curves in ascending order of phase speeds, the antisymmetric and symmetric waves are numbered as A0, A1, A2, …and S0, S1, S2, …, respectively. Analysis of the phase speed diagram (Figs. 5a,c), reveals that – with the exception of the lowest frequency curves (A0 and S0) – all the high-frequency dispersion curves of symmetric and antisymmetric waves tend to be approximately equispaced across the frequency range, and do not intersect with each other. Analysis of the group speed diagram (Figs. 5b,d), reveals that all the high-frequency dispersion curves of symmetric and antisymmetric waves show global maxima of the group speed at different finite values of frequency. By comparison, the major consequence of increasing the constitutive coupling κ consists of a general stiffening (or hardening) effect, demonstrated by systematic increments in the wavefrequencies, phase speeds and group speeds of both symmetric and antisymmetric waves.

As peculiar consequence of micropolarity, a third family of dispersion curves must be introduced. Specifically, extra dispersion branches exist that correspond to wavemodes $\boldsymbol{\psi}_{pi}(x_3, k_1)$ dominated by the modal microrotation ϑ_2, while negligibly participated by the modal displacements υ_1 and υ_3. We denote by M-family this group of *microrotational waves* (green curves), which are not encountered in classical Cauchy plates (see for instance [53]). By sorting the dispersion curves in ascending order of phase speeds, the microrotational waves are labeled as M0, M1, M2, …. As sub-classification, even-numbered waves M0, M2, M4, …differ from odd-numbered waves M1, M3, M5, …for the symmetric and antisymmetric structure of the dominant modal function $\vartheta_2(x_3)$ in the domain $\mathcal{X}_3$. Analysis of the phase speed diagram (Figs. 5a,c) reveals that, in the absence of coupling, the cutoff frequencies of micropolar modes would be exact integer multiples of the cutoff frequency of mode M1. This is due to the fact that the equation of motion is formally identical to that of shear waves in classical continua, which have the same behavior in terms of cutoff frequencies. Analysis of the group speed diagram (Figs. 5b,d) reveals that microrotational waves reach higher group speeds with respect to symmetric and antisymmetric waves, but do not show evident global maxima of the dispersion curves at finite values of frequency. The increasing of the constitutive coupling κ determines systematic increments in the wavefrequencies, phase speeds and group speeds of microrotational waves, although this effect is quantitatively lower that the hardening caused by the same κ-increment on symmetric and antisymmetric waves.

4.1.1. Low-frequency and high-frequency ranges

Low-frequency and high-frequency ranges deserve a dedicated discussion, as they can be of particular interest from a physical point of view. Within the low-frequency range top-bounded by the cutoff frequency $\omega^{\mathrm{c}}_{\mathrm{A1}}$ of the asymmetric wave A1, only waves A0, S0, M0 can propagate. As a primary remark, the frequencies $\omega_1(k_1)$ and $\omega_2(k_1)$ of waves A0 and S0 tend to zero in the limit of long wavelengths (that is, wavenumber $k_1 \to 0$). On the contrary, the frequency $\omega_3(k_1)$ of the wave M0 tends to a finite cutoff value $\omega^{\mathrm{c}}_{\mathrm{M0}}$ in the limit of long wavelengths. The phase and group speeds of waves A0, S0, M0 in the low-frequency range are reported in Fig. 6. The low-frequency diagram discloses that the phase and group speeds of wave A0 tend to zero (note that the null frequency cannot be included in the logarithmic horizontal axis), while the phase and group speeds of wave S0 tend to finite but not null values c°_{S0} and g°_{S0} in the limit of quasistatic oscillations (that is, wavefrequency $\omega \to 0$). Moreover, waves S0 show a dispersionless behavior (identical and constant phase and group speeds) over a large interval of low and very-low frequencies. After proper mathematical manipulations of the characteristic function, the phase speed limit c°_{S0} is found to be

$$c^\circ_{\mathrm{S0}} = \sqrt{\frac{(\kappa + 2\mu)(\kappa + 2\lambda + 2\mu)}{\rho(\kappa + \lambda + 2\mu)}}, \tag{38}$$

and can be referred to as *wave velocity in thin plates*, in analogy with the well-established nomenclature of classical continua. In this

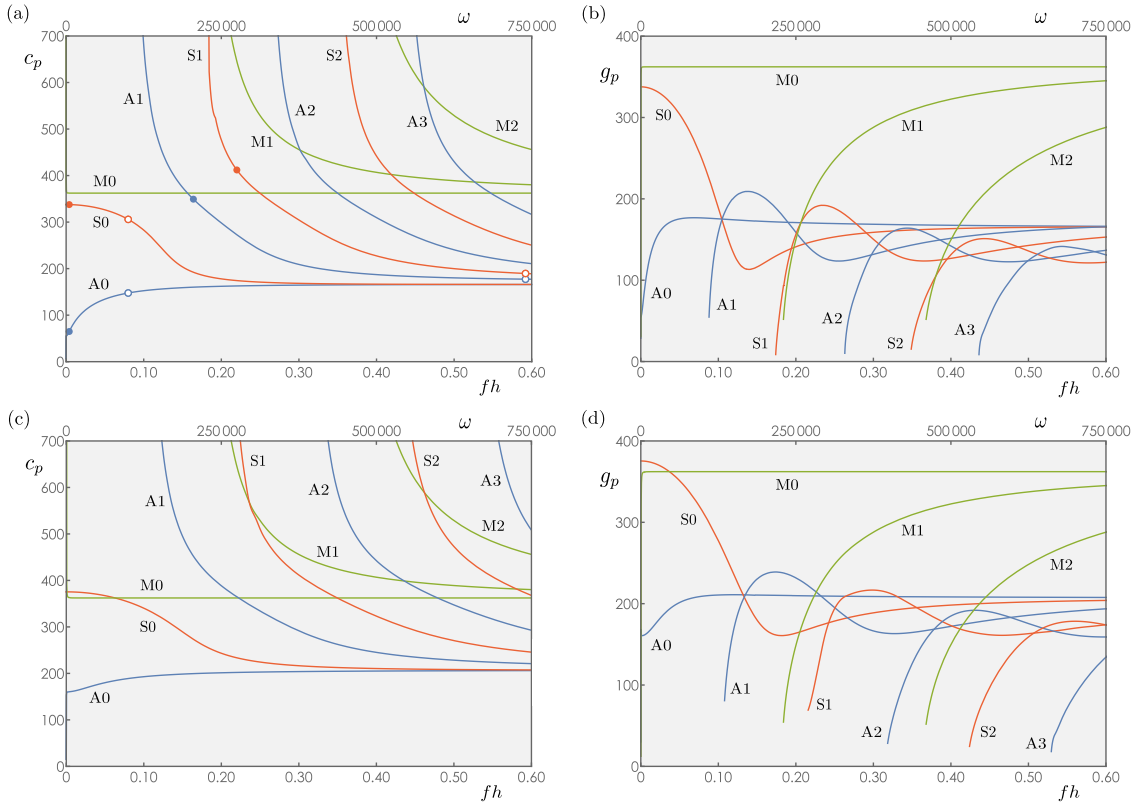

Fig. 5. Dispersion properties of in-plane guided waves propagating in the micropolar plate characterized by the parameter set $\boldsymbol{\mu}_\circ$. Dispersion diagrams show the phase velocity c_p and group velocity g_p (in [m/s]) versus frequency fh (in [mm MHz]) and circular frequency ω (in [1/rad]) for (a),(b) small coupling parameter $\kappa = 51 * 10^3$; (c),(d) large coupling parameter $\kappa = 51 * 10^4$.

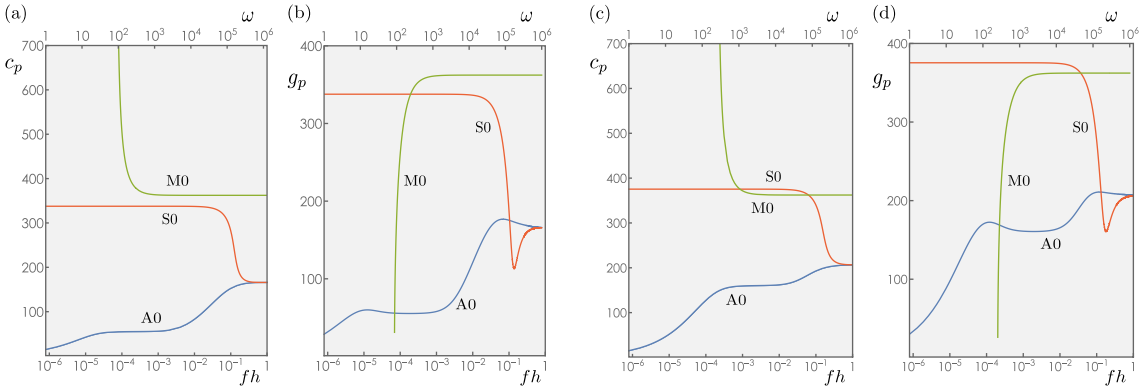

Fig. 6. Low-frequency dispersion properties of in-plane guided waves propagating in the micropolar plate characterized by the parameter set $\boldsymbol{\mu}_\circ$. Dispersion diagrams show the phase velocity c_p and group velocity g_p (in [m/s]) versus frequency fh (in [mm MHz]) and circular frequency ω (in [1/rad]) for (a),(b) small coupling parameter $\kappa = 51 * 10^3$; (c),(d) large coupling parameter $\kappa = 51 * 10^4$.

respect, it is worth remarking that the limit c°_{S0} is directly proportional to the constitutive coupling κ. It can also be verified that, if the constitutive coupling vanishes (parameter $\kappa \to 0$), the limit c°_{S0} consistently tends to the wave velocity of thin non-micropolar plates $c_{tp} = \sqrt{E/\rho(1-\nu^2)} = 2\sqrt{\mu(\lambda+\mu)/\rho(\lambda+2\mu)}$. As interesting remark related to constitutive coupling κ, the dissimilar hardening effects caused by κ-increments on the antisymmetric wave A0 (stronger hardening) and microrotational wave M0 (weaker hardening) can govern the occurrence or nonoccurrence of resonances. Indeed, A0-M0 curve intersections do not occur for low κ (Fig. 6a), whereas they do for large κ (Fig. 6c).

In the high-frequency range, all waves A and S assume a non-dispersive behavior, while their phase speeds tend to the same finite value c_s in the limit of short wavelengths (that is, wavenumber $k_1 \to \infty$, coinciding also with $\omega \to \infty$). This particular speed value can be analytically determined as $c_s = \sqrt{\kappa+\mu}/\sqrt{\rho}$. Consequently, it grows with increasing constitutive coupling κ and coincides with the limit speed c_3^∞ of *transverse displacement waves* in three-dimensional micropolar continua (see Table 1). The only exceptions to this behavior are the phase speeds of waves A0 and S0, which tend to a distinct limit value, dependent on the constitutive coupling κ and slightly lower than c_s, to be determined numerically. Similarly to symmetric and antisymmetric

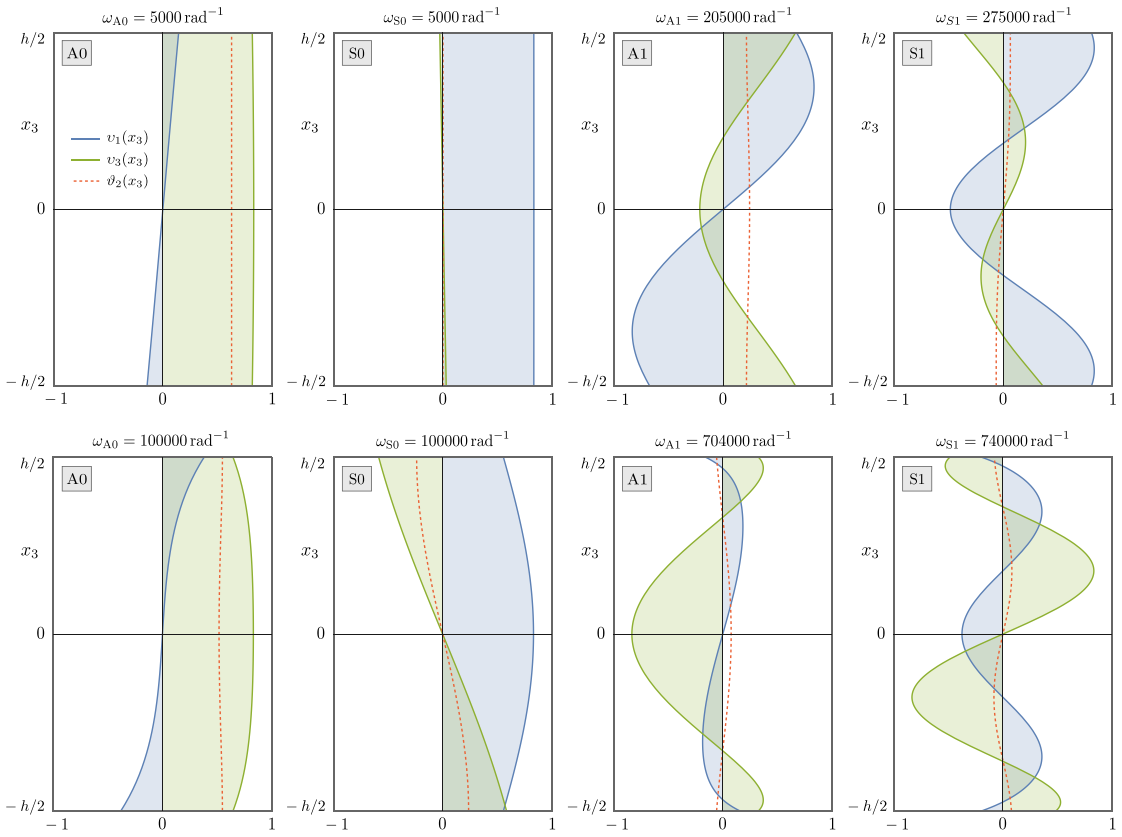

Fig. 7. Wavemodes of in-plane guided waves propagating in the micropolar plate characterized by the parameter set $\boldsymbol{\mu}_\circ$. Wavemodes A0, S0, A1 and S1 (corresponding to low or high circular frequencies ω_{A0}, ω_{S0}, ω_{A1}, ω_{S1}, respectively) dominated by the translational modal components v_1 and v_3 (continuous blue and green lines) with minimal participation of the microrotational modal component ϑ_2 (dashed red line). Dashing indicates amplification factor 10^3 (top panels) or 10^4 (bottom panels) of the modal component.

waves, microrotational waves M0, M1, M2 assume a non-dispersive behavior in the high-frequency range, while all their phase speeds tend to the same finite value c_m in the limit of short wavelengths. This particular speed value can be analytically determined as $c_m = \sqrt{\gamma}/\sqrt{\rho J}$. It is independent of the constitutive coupling κ and coincides with the limit speed c_5^∞ of *transverse microrotational waves* in three-dimensional micropolar continua (see Table 1). The physical interpretation of the asymptotic coalescence of all the wave speeds in the limit of short wavelengths is that guided waves propagating in plates with extremely short wavelengths (much smaller than the plate thickness) behave as if they were freely traveling in an unbounded three-dimensional domain.

4.2. Analysis of the wavemode structure

Although some qualitative properties of wavemodes – like symmetry and antisymmetry – persist all along a certain branch of the dispersion diagram, some other quantitative features can significantly change. Therefore, it is interesting to identify and discuss both the persistent morphology (or *modal structure*) and the changing contributions of modal components (or *polarization*) of the wavemode $\boldsymbol{\varphi}_{pi}(k_1, x_3)$ associated to the phase speed $c_{pi}(k_1)$ of the ith branch in the dispersion diagram. Discussion is focused on the lowest frequency waves A0, A1 and S0, S1, but the main findings can be extended to the respective families of antisymmetric and symmetric waves propagating at higher frequencies. Extensive parametric analyses cannot be reported here for the sake of brevity. Further investigations on the effects of variations of the constitutive coupling κ are presented in a supplementary contribution [72].

Antisymmetric waves A0, A1 are structurally characterized by the antisymmetric modal function $v_1(x_3)$ for all wavenumbers, by definition (see Fig. 7, corresponding to blue dots in Fig. 5a). Antisymmetric waves A0, A1 also show symmetric shapes of the modal functions $v_3(x_3)$ and $\vartheta_2(x_3)$. Regardless of normalization, the amplitudes of functions $v_1(x_3)$ and $v_3(x_3)$ are generally large and comparable to each other (blue and green curves), whereas the amplitude of $\vartheta_2(x_3)$ is typically lower by some orders of magnitude (amplified dashed red curve). Therefore, the A-family of waves is said to be polarized in the displacement components of motion. Considering wave A0 in the low-frequency range, the symmetric function $v_3(x_3)$ is nearly-uniform, while the antisymmetric function $v_1(x_3)$ varies quasi-linearly in the $\mathcal{X}_3$-domain, reaching minimum and maximum on the upper and lower surfaces $\mathcal{S}_u$ and $\mathcal{S}_\ell$, and attaining null value on the mid-plane $\mathcal{M}$ (see upper panel in Fig. 7, corresponding to filled blue dot in Fig. 5a). This particular morphology allows for clear identification of low-frequency waves A0 as a sort of *flexural* or *bending* waves propagating along the $\mathbf{k}_1$-direction of the plate cross-section. The increasing of frequency distorts the characteristic structure of wave A0 in a minor but not negligible manner (see lower panel in Fig. 7, corresponding to the empty blue dot in Fig. 5a). Distortions mainly occur in the proximity of the free surfaces $\mathcal{S}_u$ and $\mathcal{S}_\ell$, causing simultaneous losses of the $v_3(x_3)$-uniformity and $v_1(x_3)$-linearity. Similar qualitative and quantitative considerations hold for wave A1 and for other antisymmetric waves, which are characterized by an increasing number of modal nodes in the $\mathcal{X}_3$-domain.

Symmetric waves S0, S1 are structurally characterized by the symmetric modal function $v_1(x_3)$ for all wavenumbers, by definition (see Fig. 7). Symmetric waves S0, S1 also show antisymmetric shapes of the modal functions $v_3(x_3)$ and $\vartheta_2(x_3)$. Similarly to antisymmetric waves, amplitudes of functions $v_1(x_3)$ and $v_3(x_3)$ are generally large and comparable (blue and green curves), whereas the amplitude of $\vartheta_2(x_3)$ is typically lower by some orders of magnitude (amplified dashed red

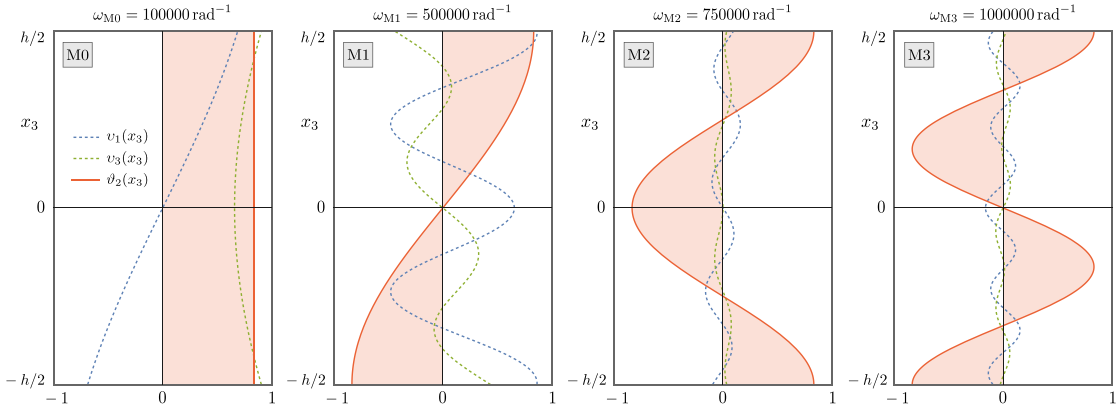

Fig. 8. Wavemodes of in-plane guided waves propagating in the micropolar plate characterized by the parameter set $\boldsymbol{\mu}_\circ$. Wavemodes M0, M1, M2 and M3 (corresponding to circular frequencies ω_{M0}, ω_{M1}, ω_{M2} and ω_{M3}, respectively) dominated by the microrotational modal component ϑ_2 (continuous red line) with minimal participation of the translational modal components v_1 and v_3 (dashed blue and green lines). Dashing indicates amplification factor 10^5 of the modal components.

curve). Therefore, the S-family of waves is said to be polarized in the displacement components of motion. Considering wave S0 in the low-frequency range, the symmetric function $v_1(x_3)$ is nearly-uniform, while the antisymmetric function $v_3(x_3)$ has very small amplitude and varies quasi-linearly in the $\mathcal{X}_3$-domain, reaching minimum and maximum on the upper and lower surfaces $\mathcal{S}_u$ and $\mathcal{S}_\ell$ and attaining null value on the mid-plane $\mathcal{M}$ (see upper panel in Fig. 7, corresponding to the filled red dot of Fig. 5a). This particular morphology allows for clear identification of low-frequency waves S0 as a sort of *extensional* or *compressional* waves propagating along the $\mathbf{k}_1$-direction of the plate section. The small $v_3(x_3)$-contribution to extensional waves can be attributed to a limited but not negligible Poisson effect. The increasing of the frequencies progressively alters the structure of wave S0 (see lower panel in Fig. 7, corresponding to empty red dot in Fig. 5a). Alterations mainly occur in the proximity of the free surfaces $\mathcal{S}_u$ and $\mathcal{S}_\ell$, where losses of the $v_1(x_3)$-uniformity happen. Simultaneously, the participation of the modal function $v_1(x_3)$ grows, due to the increasing role of the Poisson effect. Similar qualitative and quantitative considerations can be carried out for wave S1 and other symmetric waves, which are characterized by an increasing number of modal nodes in the $\mathcal{X}_3$-domain.

In the very high frequency range, the structure of both antisymmetric and symmetric waves A1 and S1 tends to be increasingly dominated by the modal function $v_3(x_3)$, with high amplitudes attained in the proximity of the free surfaces $\mathcal{S}_u$ and $\mathcal{S}_\ell$. This particular morphology is coherent with the trend of the respective phase speeds, both converging to the limit c_3^∞ of transverse displacement waves in the limit of short wavelengths (that is, wavenumber $k_1 \to \infty$ or $\omega \to \infty$).

The minimal participation of the microrotational modal function $\vartheta_2(x_3)$ causes the modal structures of antisymmetric waves A0, A1 and symmetric waves S0, S1 propagating in the micropolar plates to resemble those of waves propagating in classical plates, at least in the absence of resonance conditions. In contrast, the modal structure of microrotational waves is a peculiar and unique feature to micropolar plates. Remarkably, the modal structure of microrotational waves, exemplified in Fig. 8 for a particular set of frequencies, is quasi-independent of the frequency or wavenumber. In particular, microrotational waves M0, M2 are dominated by symmetric modal function $\vartheta_2(x_3)$ (red curves), but also participated by antisymmetric modal function $v_1(x_3)$ (dashed blue curve) and by symmetric modal function $v_3(x_3)$ (dashed green curve) with very low amplitudes. Wave M0, in particular, shows nearly-uniform modal function $\vartheta_2(x_3)$. In contrast, microrotational waves M1, M3 are dominated by antisymmetric modal function $\vartheta_2(x_3)$ (red curves), while participated by symmetric modal function $v_1(x_3)$ (dashed blue curve) and by antisymmetric modal function $v_3(x_3)$ (dashed green curve) with very low amplitudes. Therefore, the M-family of waves is said to be polarized in the microrotation component of motion. Modal structures similar to M1 and M2 characterize all the other even-numbered and odd-numbered microrotational waves, respectively, except for the increasing number of modal nodes in the $\mathcal{X}_3$-domain.

4.3. Resonance and nearly-resonance conditions

Resonance or nearly resonance conditions may occur in the dispersion spectrum if the characteristic equation $F_p(\omega, k_1) = 0$ has a double solution $\omega_{pi}(k_1)$ or a pair of close solutions $\omega_{pi}(k_1)$ and $\omega_{pj}(k_1)$ for a particular wavenumber k_1. This mathematical condition corresponds to the intersection or quasi-intersection of two different branches of the dispersion diagram. Within the eigensensitivity analysis of linear systems, it is known that two eigenvalue loci can approach to each other under variation of one or more governing parameters. The mutual interplay among the two approaching eigenvalue loci can result in an intersection of the loci curves (*crossing* or *crossover phenomenon*) or in a sudden repulsion of the loci curves, which veer away from each other with high and opposite curvatures (*avoided crossing* or *veering phenomenon*). The minimal distance reached by two veering loci is usually referred to as the veering amplitude. Morphologically, the strong local interaction causes the eigenfunctions associated with the veering eigenvalues interchange their morphologies in a rapid but continuous way (*hybridization phenomenon*). In solids and structural mechanics, crossing and veering are considered fascinating and interesting dynamic phenomena. Indeed, from the mathematical viewpoint, veering regions correspond to the largest eigenvalue and eigenvector sensitivities in the parameter space. Also, from the physical viewpoint, crossings and veerings open the possibility for significant energy exchanges between the associated resonant or quasi-resonant eigenfunctions. Veering phenomena, in particular, have been observed and studied in a number of mechanical systems, either as effect of symmetry-breaking and periodicity-disturbing perturbations [73–76], or as natural consequence of the interaction between symmetric and antisymmetric modes [77–81]. The mechanical system under investigation falls into this latter class.

From a mechanical perspective, intersections between two branches of the dispersion diagram of micropolar plates occur due to strong differences in the group speeds of *slower* antisymmetric and symmetric waves and *faster* microrotational waves (upper-left panel of Fig. 9). Within the wave dynamics of dispersive elastic media, the convergence of two distinct spectral branches with different group speeds can be considered a recurrent scenario, described in coupled waveguides [82],

non-micropolar orthorhombically-anisotropic plates [55], stratified or layered systems [83], and generalized continua [84]. Nonetheless, it may be worth noting that this scenario differs from other typical mechanisms of bimodal interaction, such as (i) the interplay between two spectral branches converging to each other with opposite-sign group speeds, causing the veering phenomenon between an ordinary (stiff) acoustic phonon mode with a back-folded (soft) phonon mode, which may result is zero group speed points and the roton-like behavior observed in nonlocal crystals, nonlinear magnetic lattices and mono/multimode metamaterials [85–87], or (ii) the interplay between two spectral branches converging to each other with positive and null group speeds, causing the veering phenomenon between an ordinary acoustic phonon mode and a flat-band resonator mode, which determines the polariton-like behavior characteristic of locally resonant metamaterials [88–90]. In the micropolar plate, as a consequence of the different growth rates of distinct frequencies $\omega_{pi}(k_1)$, a number of resonance or quasi-resonance conditions can be identified (dots in the upper-left panel of Fig. 9). Local analyses in the resonant regions allow to distinguish crossing phenomena (gray-filled circles) from veering phenomena (white-filled circles). Four relevant instances of crossing and veering phenomena are considered (upper-left panels of Fig. 9):

- crossing C1 involving the pair M0 and S1,
- crossing C2 involving the pair M1 and A2,
- veering V1 involving the pair M0 and A1,
- veering V2 involving the pair M0 and S2,

with an analysis of the corresponding wavemodes (lower panels of Fig. 9). Before discussing the waveforms, it may be worth remarking that both the number and position of the resonant regions in the dispersion diagram depend on the selected combination of parameters. Focusing on the constitutive coupling κ, in particular, increments of the parameter κ can generate additional veering phenomena, characterized by large amplitudes and centered in low frequencies (for instance between waves M1 and S1). Furthermore, parametric analyses disclose that increasing the parameter κ can significantly enlarge all the veering amplitudes [72].

Perfectly resonant wavemodes at crossings C1 and C2 do not interact across the intersection of their dispersion curves. Consequently, they maintain unchanged their respective modal structures, characterized by displacement polarization (waves S1 and A2) and microrotation polarization (waves M0 and M1). Similar considerations are valid for the structures and polarizations of all the other pairs of wavemodes involved in crossing phenomena.

Differently, the pairs of quasi resonant wavemodes at veerings V1 and V2 strongly interact with each other. In fact, the two veering wavemodes undergo a complete hybridization process, which consists of a progressive swap of their respective morphologies, until the complete exchange of the modal functions. Consequently, the hybridization process of a veering wavemode implies its complete depolarization and repolarization (with the polarization of the other wavemode). Since the process develops continuously, the two veering waves assume every possible degree of hybridization in the narrow region of quasi-resonance. Generally, the highest level of hybridization corresponds to the minimal distance between the dispersion curves [76,91]. As a paradigmatic example, the higher-frequency wave A1 (blue curve) and lower-frequency wave M0 (green curve) enter the veering region V1 (top right panel of Fig. 9) with strong displacement polarization and microrotation polarization, respectively. As their respective dispersion curves approach each other, the wavemodes start hybridizing (blended color curves), until the maximum hybridization corresponding to the minimum inter-curve distance is reached. The structures of hybrid wavemodes H1a and H1b at maximal hybridization show the same modal functions $v_1(x_3)$ and $v_3(x_3)$ combined with identical but opposite-signed modal function $\vartheta_2(x_3)$. All the modal functions participate in the hybrid wavemode with comparable amplitudes (depolarization). Beyond the zone of maximum hybridization, the wavemodes complete the swap of their respective morphologies (repolarization) and leave the veering zone as lower-frequency wave A1 and higher-frequency wave M0 (exchanged polarizations). The same considerations can be extended to the structures and polarizations of the hybrid wavemodes H2a and H2b at veering V2 and all the other pairs of hybrid modes involved in veering phenomena. As a minor remark, the veering amplitudes tend to decrease for the veering phenomena occurring at higher frequencies (like those between M0 and A3, or M2 and A3).

The general scenario of interplaying dispersion curves deserves an investigation specifically aimed at identifying the physical-mathematical conditions that activate the modal interactions responsible for crossing or veering phenomena. The previous discussion clearly highlighted that the activation depends on the relative structure of the resonant wavemodes. Therefore, by taking inspiration from the well-established conditions for activating super-harmonic and sub-harmonic interactions in nonlinear dynamics [92], the occurrence of crossing or veering can be related to the orthogonality or non-orthogonality between the wavemodes, respectively. A proper orthogonality factor can be defined as

$$\Gamma_{ij}(k_1) = \int_{\mathcal{X}_3} \boldsymbol{\varphi}^{\dagger}_{pi}(x_3,k_1)\cdot\boldsymbol{\varphi}_{pj}(x_3,k_1)\,dx_3. \tag{39}$$

Regardless of the particular wavenumber k_1, the orthogonality factor Γ_{ij} can be verified to systematically attain: (i) null value (orthogonality) for non-interacting pairs of waveforms $\boldsymbol{\varphi}^{*}_{pi}$ and $\boldsymbol{\varphi}_{pj}$ in crossing dispersion curves, or (ii) non-null value (non-orthogonality) for interacting pairs of waveforms $\boldsymbol{\varphi}^{*}_{pi}$ and $\boldsymbol{\varphi}_{pj}$ in veering dispersion curves. According to this evidence, it can be conjectured that the dispersion curves of orthogonal wavemodes cross, while those of non-orthogonal wavemodes veer. Furthermore, the condition of non-orthogonality enables the process of modal hybridization.

5. Conclusions

A comprehensive analysis of the free propagation of harmonic bulk and guided waves in micropolar plates, modeled as homogeneous and isotropic finite-thickness layers of the non-dissipative three-dimensional Cosserat continuum, has been presented. By adopting the linear theory of micropolar elasticity and solving the governing equations in the frequency–wavenumber domain, the mathematical results and their physical interpretation have uncovered a variety of distinctive wave phenomena associated with the enriched kinematics and couple-traction interactions of the medium.

Concerning first bulk waves propagating in unbounded micropolar solids, an original spectral decomposition of the acoustic tensor has been provided. The related eigenproblem has been analytically solved to obtain the complete dispersion relations, including wavefrequencies, waveforms, phase and group speeds. Within the analysis of the dispersion properties in the ranges of very-high and very-low wavelengths, the limits of the phase speed have been reviewed. A complementary but novel advance has been achieved from the methodological viewpoint, by the introduction of energy-based polarization factors, which enable a precise qualitative and quantitative classification of transverse waveforms according to their dominant kinematic nature — whether translational or microrotational. Specifically, the existence of maxima and minima in the contributions of translations or microrotations to the propagating waves has been discovered in the range of long wavelengths. Analytical formulas have been provided for the positions of these extrema, corresponding to the largest microroto-translational coupling, in the wavenumber domain.

Guided waves propagating harmonically in micropolar plates have been investigated through the partial wave technique. After analytically verifying the possibility of fully decoupling the in-plane and off-plane problems, the analysis focused on in-plane waves, while the study of

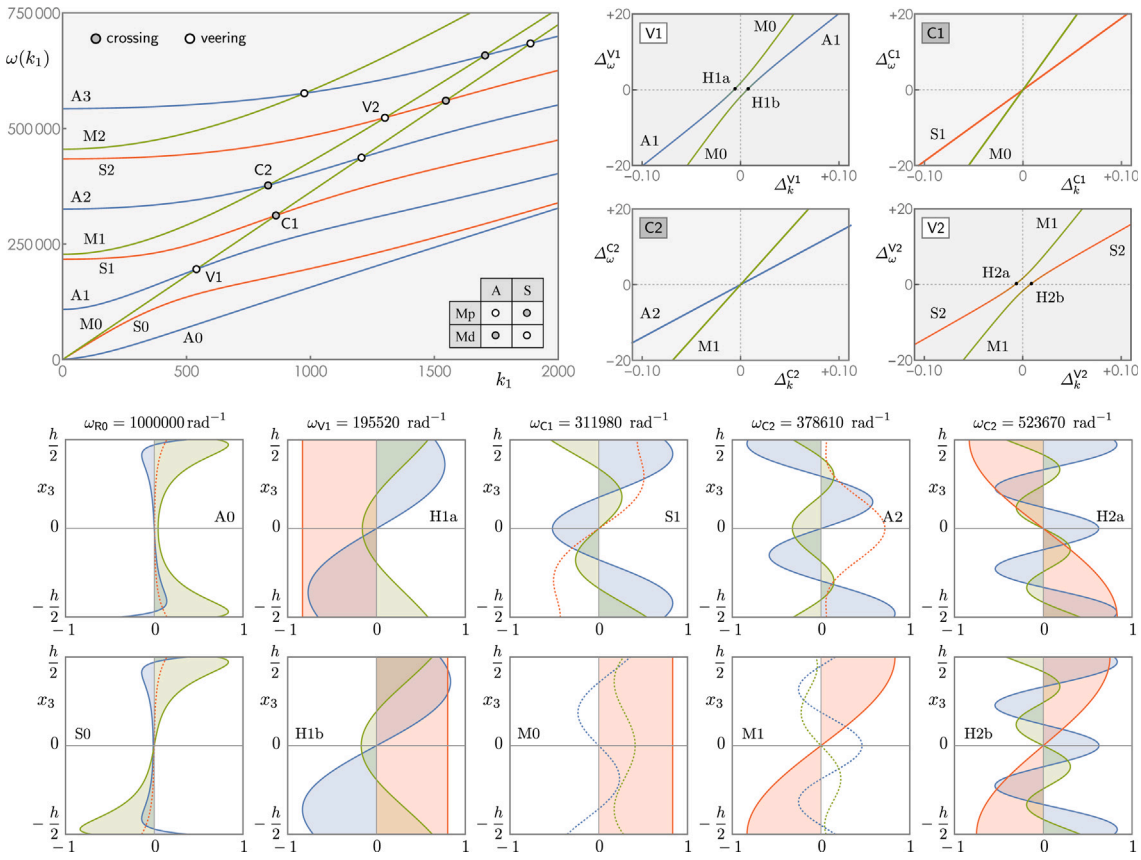

Fig. 9. Resonance and nearly-resonance conditions of in-plane guided waves propagating in the micropolar plate characterized by the parameter set $\boldsymbol{\mu}_\circ$. Dispersion diagram showing the circular frequency ω (in [1/rad]) versus wavenumber k_1 (in [rad/m]) with classification of crossing and veering phenomena (top left panel). Windows of the dispersion diagram centered at crossings C1 and C2 and veerings V1 and V2 (top right panel, where $\Delta^{\mathsf{J}}_{\omega} = \omega - \omega_{\mathsf{J}}$ and $\Delta^{\mathsf{J}}_{k} = k_1 - k_{\mathsf{J}}$ with $\mathsf{J} = \mathsf{C1}, \mathsf{C2}, \mathsf{V1}, \mathsf{V2}$). Pairs of polarized wavemodes at the nearly resonance R0 and crossings C1 and C2, pairs of hybrid wavemodes at veerings V1 and V2 (bottom panels).

off-plane waves will be the subject of future research. The dispersion relations have been derived by stating a sequence of two parametric algebraic eigenproblems: while the first could be solved analytically, the second required numerical continuation algorithms of the solutions. Nonetheless, the limiting values of phase and group speeds of guided waves have been determined in a parametric analytical form, offering a significant original contribution to the understanding of how micropolar effects modify classical wave behavior. This study has further displayed several unexplored dynamic phenomena, showing that the dispersion spectrum is significantly richer than in classical elasticity, owing to the emergence of additional spectral branches associated with pure rotational (micropolar) wavemodes. These micropolar branches are characterized by nearly equispaced cutoff frequencies and generally propagate with high phase speeds. The family of micropolar branches not only broadens the taxonomy of propagating waves, but also interplays with the classical families of spectral branches, giving rise to complex mechanisms of linear modal interaction, such as crossing and veering phenomena. As significant original contribution, a proper geometrical criterion of modal orthogonality has been defined to analytically predict the occurrence of veering (or crossing) phenomena at the intersection of two spectral branches. Veering phenomena, indeed, determine quasi-resonance conditions and activate local hybridization mechanisms between wavemodes belonging to distinct wave families. Consequently, the strong modal interactions between hybrid wavemodes can favor the transfer of mechanical energy across the interacting branches.

All the dynamic phenomena have been investigated with the primary objective of understanding and discussing how dispersion characteristics, cutoff frequencies, wavemode morphology, crossings and veerings are affected by the constitutive parameters of the micropolar continuum, especially the coupling modulus of the material. Clarifying these aspects offers promising perspectives for exciting the micropolar response and applying inverse identification procedures, in which dynamic wave measurements could be used to estimate the elusive micropolar constitutive parameters.

CRediT authorship contribution statement

Annamaria Pau: Writing – review & editing, Writing – original draft, Visualization, Validation, Software, Methodology, Investigation, Formal analysis, Data curation, Conceptualization. **Marco Lepidi:** Writing – review & editing, Writing – original draft, Visualization, Validation, Software, Methodology, Investigation, Formal analysis, Data curation, Conceptualization.

Declaration of competing interest

The authors declare that they have no known competing financial interests or personal relationships that could have appeared to influence the work reported in this paper.

Appendix

A.1. Mathematical concepts and notation

A.1.1. Axial vector

Set $\mathbb{R}^3$, considered as a Lie algebra with the commutator given by the cross product, is isomorphic to $\mathfrak{so}(3,\mathbb{R})$, which is the group of

antisymmetric three-by-three matrices. Let $\phi : \mathfrak{so}(3,\mathbb{R}) \to \mathbb{R}^3$ be this isomorphism. Its action on $\mathbb{R}^3$ is identified with the action of $\mathbb{R}^3$ on itself given by the cross-product

$$\mathbf{A}\mathbf{v} = \phi(\mathbf{A}) \times \mathbf{v}, \tag{40}$$

where $\mathbf{A} \in \mathfrak{so}(3,\mathbb{R})$ and $\mathbf{v} \in \mathbb{R}^3$. The element $\phi(\mathbf{A}) \in \mathbb{R}^3$ is the *axial vector* [93].

A.1.2. Algebraic and differential operators

The following component relationships hold in the algebraic and differential treatment of vectors, tensors and matrices

$$\begin{aligned} &(\mathrm{sym}(\mathbf{A}))_{ij} = 1/2(A_{ij} + A_{ji}), && (\mathrm{skew}(\mathbf{A}))_{ij} = 1/2(A_{ij} - A_{ji}), \\ &(\nabla \mathbf{v})_{ij} = v_{i,j}, && (\nabla^2 \mathbf{v})_i = v_{i,ii} + v_{i,jj} + v_{i,kk}, \\ &(\mathrm{curl}\, \mathbf{v})_i = (-1)^{(i-1)}(v_{k,j} - v_{j,k}), && (\mathrm{div}\, \mathbf{A})_i = \textstyle\sum_j A_{ij,j}, \end{aligned} \tag{41}$$

where $\mathbf{v}$ is a three-by-one vector and $\mathbf{A}$ is a three-by-three tensor, and the subscript indexes preceded by a comma represents partial differentiation with respect to space variables.

A.2. Auxiliary matrices

The auxiliary matrices needed to relate the displacement vector $\mathbf{u}$ and microrotation vector θ with the in-plane and out-plane displacement–microrotational vectors $\mathbf{p}$ and $\mathbf{q}$ have the Boolean form

$$\begin{aligned} \mathbf{B}_{up} &= \begin{bmatrix} 1 & 0 & 0 \\ 0 & 0 & 0 \\ 0 & 1 & 0 \end{bmatrix}, \quad \mathbf{B}_{uq} = \begin{bmatrix} 0 & 0 & 0 \\ 1 & 0 & 0 \\ 0 & 0 & 0 \end{bmatrix}, \\ \mathbf{B}_{\theta p} &= \begin{bmatrix} 0 & 0 & 0 \\ 0 & 0 & 1 \\ 0 & 0 & 0 \end{bmatrix}, \quad \mathbf{B}_{\theta q} = \begin{bmatrix} 0 & 1 & 0 \\ 0 & 0 & 0 \\ 0 & 0 & 1 \end{bmatrix}. \end{aligned} \tag{42}$$

Data availability

Data will be made available on request.

References

[1] Cosserat E, Cosserat F. Théorie des corps déformables. A. Hermann et fils; 1909.
[2] Erofeyev VI. Wave processes in solids with microstructure. World Scientific Publishing; 2003.
[3] Green AE, Rivlin RS. Multipolar continuum mechanics. Arch Ration Mech Anal 1964;17:113–47.
[4] Mindlin RD. On the equations of elastic materials with micro-structure. Int J Solids Struct 1965;1(1):73–8.
[5] Truesdell C, Noll W. The nonlinear field theories of mechanics. In: Flügge S, editor. Handbuch der Physik, vol. III. Berlin: Springer; 1965.
[6] Forest S, Sab K. Cosserat overall modeling of heterogeneous materials. Mech Res Commun 1998;25(4):449–54.
[7] Ehlers W, Ramm E, Diebels S, d'Addetta GA. From particle ensembles to Cosserat continua: homogenization of contact forces towards stresses and couple stresses. Int J Solids Struct 2003;40(24):6681–702.
[8] Goddard JD. Continuum modeling of granular media. Appl Mech Rev 2014;66(5):050801.
[9] Hassanpour S, Heppler GR. Micropolar elasticity theory: A survey of linear isotropic equations, representative notations, and experimental investigations. Math Mech Solids 2017;22(2):224–42.
[10] Bigoni D, Drugan WJ. Analytical derivation of Cosserat moduli via homogenization of heterogeneous elastic materials. ASME J Appl Mech 2006;74(4):741–53.
[11] Pau A, Trovalusci P. A multifield continuum model for the description of the response of microporous/microcracked composite materials. Mech Mater 2021;160:103965.
[12] Ogam E, Fellah ZEA, Fellah M, Depollier C. Theoretical and experimental study of micropolar elastic materials using acoustic waves in air. J Sound Vib 2021;510:116298.
[13] Diebels S, Geringer A. Micromechanical and macromechanical modelling of foams: Identification of Cosserat parameters. ZAMM-Journal Appl Math Mechanics/Zeitschrift Für Angew Math Und Mech 2014;94(5):414–20.
[14] Bažant ZZ, Christensen M. Analogy between micropolar continuum and grid frameworks under initial stress. Int J Solids Struct 1972;8(3):327–46.
[15] Pau A, Trovalusci P. Block masonry as equivalent micropolar continua: the role of relative rotations. Acta Mech 2012;223(7):1455–71.
[16] Yang JFC, Lakes RS. Experimental study of micropolar and couple stress elasticity in compact bone in bending. J Biomech 1982;15(2):91–8.
[17] Shaat M, Gao X-L. Constitutive modeling of mechanical coupling in 2D biomimetic metamaterials with chirality, anisotropy and non-centrosymmetry. Int J Mech Sci 2025;295:110276.
[18] Mehta VK, Srinivasa AR, Reddy J. Energy equivalence-based homogenized micropolar model for 2D high valency architected materials: Periodic, semi-periodic, and aperiodic. Mech Res Commun 2025;149:104530.
[19] Spadoni A, Ruzzene M. Elasto-static micropolar behavior of a chiral auxetic lattice. J Mech Phys Solids 2012;60(1):156–71.
[20] Gad AI, Gao XL, Li K. A strain energy-based homogenization method for 2-D and 3-D cellular materials using the micropolar elasticity theory. Compos Struct 2021;265:113594.
[21] Diana V, Bacigalupo A, Gambarotta L. Continuum-molecular modeling of planar micropolar media: Anisotropy, chiral properties and length-scale effects. Int J Solids Struct 2024;295:112810.
[22] Ulloa J, Ariza M, Andrade J, Ortiz M. Homogenized models of mechanical metamaterials. Comput Methods Appl Mech Engrg 2025;433:117454.
[23] Lakes RS. Cubic lattice rib shape: tuning of Poisson's ratio and Cosserat characteristic length. Phys Status Solidi (B) 2025;2500330.
[24] Novacki W. Theory of asymmetric elasticity. Pergamon Press; 1986.
[25] Eringen AC. Microcontinuum field theories I: Foundations and Solids. Springer; 1999.
[26] Suiker ASJ, Metrikine AV, De Borst R. Comparison of wave propagation characteristics of the Cosserat continuum model and corresponding discrete lattice models. Int J Solids Struct 2001;38(9):1563–83.
[27] Chen Y, Frenzel T, Guenneau S, Kadic M, Wegener M. Mapping acoustical activity in 3D chiral mechanical metamaterials onto micropolar continuum elasticity. J Mech Phys Solids 2020;137:103877.
[28] Bacigalupo A, Gambarotta L, Lepidi M. Thermodynamically consistent non-local continualization for masonry-like systems. Int J Mech Sci 2021;205:106538.
[29] Eskandari S, Xu W, Chen S, Abali BE, Orsat V, Akbarzadeh A. Elastic-wave propagation in chiral metamaterials: A couple-stress theory perspective. Adv Eng Mater 2025;27(9):2402299.
[30] Kishine J, Ovchinnikov A, Tereshchenko A. Chirality-induced phonon dispersion in a noncentrosymmetric micropolar crystal. Phys Rev Lett 2020;125(24):245302.
[31] Chen Y, Schneider JL, Groß MF, Wang K, Kalt S, Scott P, et al. Observation of chirality-induced roton-like dispersion in a 3D micropolar elastic metamaterial. Adv Funct Mater 2024;34(20):2302699.
[32] Truesdell C, Toupin R. The classical field theories. In: Principles of classical mechanics and field theory/Prinzipien der klassischen Mechanik und Feldtheorie. Springer; 1960, p. 226–858.
[33] Grioli G. Elasticità asimmetrica. Ann di Mat Pura Ed Appl 1960;50(1):389–417.
[34] Mindlin RD, Tiersten H. Effects of couple-stresses in linear elasticity. Arch Ration Mech Anal 1962;11(1):415–48.
[35] Toupin R. Elastic materials with couple-stresses. Arch Ration Mech Anal 1962;11(1):385–414.
[36] Günther W. Zur Statik und Kinematik des Cosseratschen Kontinuums. Abh der Braunschweigschen Wiss Ges 1958;10(213):196–213.
[37] Aero E, Kuvshinskii E. Fundamental equations of the theory of elastic media with rotationally interacting particles. Sov Physics-Solid State 1961;2(7):1272–81.
[38] Pal'mov V. Fundamental equations of the theory of asymmetric elasticity. J Appl Math Mech 1964;28(3):496–505.
[39] Eringen AC. Linear theory of micropolar elasticity. J Math Mech 1966;909–23.
[40] Schaefer H. Das Cosserat Kontinuum. ZAMM-Zeitschrift Für Angew Math Und Mech 1967;47(8):485–98.
[41] Ieşan D. On the linear theory of micropolar elasticity. Internat J Engrg Sci 1969;7(12):1213–20.
[42] Pasternak E, Dyskin AV. On a possibility of reconstruction of Cosserat moduli in particulate materials using long waves. Acta Mech 2014;225(8):2409–22.
[43] Gauthier RD, Jahsman WE. A quest for micropolar elastic constants. J Appl Mech 1975;42(2):369–74.
[44] Jahsman W, Gauthier R. Dynamic measurements of micropolar elastic constants. In: Continuum models of discrete systems. Ontario, Canada: University of Waterloo Press; 1980.
[45] Gauthier RD. Experimental investigations on micropolar media. Mech Micropolar Media 1982;1:395–463.
[46] Lakes RS. Experimental evaluation of micromorphic elastic constants in foams and lattices. ZAMP-Zeitschrift Für Angew Math Und Phys 2023;74(1):31.
[47] Parfitt VR, Eringen AC. Reflection of plane waves from the flat boundary of a micropolar elastic half-space. J Acoust Soc Am 1969;45(5):1258–72.
[48] Kulesh MA, Matveenko VP, Ulitin MV, Shardakov I. Analysis of the wave solution of the elastokinetic equations of a Cosserat continuum for the case of bulk plane waves. J Appl Mech Tech Phys 2008;49(2):323–9.
[49] Kulesh M, Grekova EF, Shardakov I. The problem of surface wave propagation in a reduced Cosserat medium. Acoust Phys 2009;55(2):218–26.

[50] Grekova EF. Plane waves in the linear elastic reduced Cosserat medium with a finite axially symmetric coupling between volumetric and rotational strains. Math Mech Solids 2016;21(1):73–93.
[51] Gauthier RD, Jahsman WE. A quest for micropolar elastic constants. Part II. Arch Mech 1981;33(5):717–37.
[52] Kulesh MA, Matveenko VP, Shardakov I. Constructing an analytical solution for lamb waves using the Cosserat continuum approach. J Appl Mech Tech Phys 2007;48(1):119–25.
[53] Rose JL. Ultrasonic guided waves in solid media. Cambridge University Press; 2014.
[54] Auld BA. Acoustic fields and waves in solids. John Wiley and Sons; 1973.
[55] Nobili A, Erbaş B, Signorini C. Veering of Rayleigh-Lamb waves in orthorhombic materials. Math Mech Solids 2022;27(9):1783–99.
[56] Manconi E, Sorokin S. On the effect of damping on dispersion curves in plates. Int J Solids Struct 2013;50(11–12):1966–73.
[57] Quintanilla FH, Lowe M, Craster R. Full 3D dispersion curve solutions for guided waves in generally anisotropic media. J Sound Vib 2016;363:545–59.
[58] Zhu F, Wang B, Qian Z, Pan E. Accurate characterization of 3D dispersion curves and mode shapes of waves propagating in generally anisotropic viscoelastic/elastic plates. Int J Solids Struct 2018;150:52–65.
[59] Solie LP, Auld BA. Elastic waves in free anisotropic plates. J Acoust Soc Am 1973;54(1):50–65.
[60] Pau A, Lanza Di Scalea F. Nonlinear guided wave propagation in prestressed plates. J Acoust Soc Am 2015;137(3):1529–40.
[61] Hakoda C, Lissenden CJ. Using the partial wave method for wave structure calculation and the conceptual interpretation of elastodynamic guided waves. Appl Sci 2018;8(6):966.
[62] Kafadar CB, Eringen AC. Micropolar media — I the classical theory. Internat J Engrg Sci 1971;9(3):271–305.
[63] Dyszlewicz J. Micropolar theory of elasticity, vol. 15. Springer Science & Business Media; 2004.
[64] Eremeyev VA, Lebedev LP, Altenbach H. Foundations of micropolar mechanics. Springer Science & Business Media; 2012.
[65] Pietraszkiewicz W, Eremeyev VA. On vectorially parameterized natural strain measures of the non-linear Cosserat continuum. Int J Solids Struct 2009;46(11–12):2477–80.
[66] Lakes RS. Colloquium: Materials that exceed classical thermodynamic bounds on properties. Rev Modern Phys 2025;97(2):021002.
[67] Hussein MI, Leamy MJ, Ruzzene M. Dynamics of phononic materials and structures: Historical origins, recent progress, and future outlook. Appl Mech Rev 2014;66(4):040802.
[68] Bacigalupo A, Lepidi M. Acoustic wave polarization and energy flow in periodic beam lattice materials. Int J Solids Struct 2018;147:183–203.
[69] Wang M, Pau A, Lepidi M. Elastoacoustic wave propagation in a biphasic mechanical metamaterial. J Acoust Soc Am 2024;155(5):3322–35.
[70] Arena A, Lepidi M. Nonlinear wave propagation in a two-dimensional lattice model of textile metamaterials. Nonlinear Dynam 2025;113:23863–84.
[71] Pau A, Meso C, Fellah ZEA, Erick O. Acoustic wave transmission of micropolar plates. In: Proc. of 6th ECCOMAS thematic conference on uncertainty quantification in computational sciences and engineering UNCECOMP 2025. 2025.
[72] Pau A, Lepidi M. Dispersion properties of micropolar plates through the partial wave technique. In: Chang F-K, Guemes A, editors. Structural health monitoring 2025. Ensuring mobility and autonomy with sustainability. DEStech Publications; 2025, p. 1287–94.
[73] Perkins NC, Mote C. Comments on curve veering in eigenvalue problems. J Sound Vib 1986;106(3):451–63.
[74] Pierre C. Mode localization and eigenvalue loci veering phenomena in disordered structures. J Sound Vib 1988;126(3):485–502.
[75] Luongo A. Eigensolutions of perturbed nearly defective matrices. J Sound Vib 1995;185(3):377–95.
[76] Lepidi M. Multi-parameter perturbation methods for the eigensolution sensitivity analysis of nearly-resonant non-defective multi-degree-of-freedom systems. J Sound Vib 2013;332(4):1011–32.
[77] Triantafyllou M, Triantafyllou G. Frequency coalescence and mode localization phenomena: a geometric theory. J Sound Vib 1991;150(3):485–500.
[78] Vidoli S, Vestroni F. Veering phenomena in systems with gyroscopic coupling. ASME J Appl Mech 2004;72(5):641–7.
[79] Lacarbonara W, Paolone A, Vestroni F. Elastodynamics of nonshallow suspended cables: Linear modal properties. ASME J Vib Acoust 2007;129(4):425–33.
[80] Lepidi M, Gattulli V. A parametric multi-body section model for modal interactions of cable-supported bridges. J Sound Vib 2014;333(19):4579–96.
[81] Gattulli V, Lepidi M, Potenza F, Di Sabatino U. Dynamics of masonry walls connected by a vibrating cable in a historic structure. Meccanica 2016;51(11):2813–26.
[82] Mace BR, Manconi E. Wave motion and dispersion phenomena: Veering, locking and strong coupling effects. J Acoust Soc Am 2012;131(2):1015–28.
[83] Kuznetsov S. Lamb waves in three-layered plates: crossing fundamental branches and wave bifurcation. Acta Mech 2024;235(6):4057–65.
[84] Settimi V, Trovalusci P, Rega G. Dynamical properties of a composite microcracked bar based on a generalized continuum formulation. Contin Mech Thermodyn 2019;31(6):1627–44.
[85] Groß MF, Schneider JL, Chen Y, Kadic M, Wegener M. Dispersion engineering by hybridizing the back-folded soft mode of monomode elastic metamaterials with stiff acoustic modes. Adv Mater 2024;36(6):2307553.
[86] Samak MM, Bilal OR. Evidence of zero group velocity at the lowest dispersion branch through local interactions. APL Mater 2024;12(1):011111.
[87] Wang K, Schneider JL, Chen Y, Martínez JAI, Kadic M, Wang C. Roton dispersion and displacement oscillatory for a nonlocal mechanical system. Eur J Mech A Solids 2025;115:105842.
[88] Lepidi M, Bacigalupo A. Multi-parametric sensitivity analysis of the band structure for tetrachiral acoustic metamaterials. Int J Solids Struct 2018;136:186–202.
[89] Beli D, Ruzzene M, De Marqui Jr C. Bridging-coupling phenomenon in linear elastic metamaterials by exploiting locally resonant metachain isomers. Phys Rev Appl 2020;14(3):034032.
[90] Zhou X, Chen Y, Zhang J, Cao S, Yang X, Ren L, et al. Multifunctional bioinspired acoustic metamaterials with tunable phonon bandgap. Int J Mech Sci 2025;304:110707.
[91] du Bois JL, Adhikari S, Lieven NAJ. On the quantification of eigenvalue curve veering: A veering index. ASME J Appl Mech 2011;78(4):041007.
[92] Lacarbonara W, Rega G, Nayfeh A. Resonant non-linear normal modes. Part I: analytical treatment for structural one-dimensional systems. Int J Non-Linear Mech 2003;38(6):851–72.
[93] Kirillov A. Introduction to Łie groups and Łie algebras. Cambridge University Press; 2008.